

Supersoft X-Ray Nebulae in the Large Magellanic Cloud

Diego A. Farias,^{1,2*} Alejandro Clocchiatti,^{1,2} Tyrone E. Woods³ and Armin Rest⁴

¹*Institute of Astrophysics, Universidad Católica de Chile, Santiago, Chile*

²*Millennium Institute of Astrophysics (MAS), Santiago, Chile*

³*National Research Council of Canada, Herzberg Astronomy & Astrophysics Research Centre, 5071 West Saanich Road, Victoria, BC V9E 2E7, Canada*

⁴*Space Telescope Science Institute, 3700 San Martin Drive, Baltimore, MD 21218, USA*

Accepted 2020 July 21. Received 2020 July 14; in original form 2020 May 25

ABSTRACT

Supersoft X-rays sources (SSSs) have been proposed as potential Type Ia supernova (SN Ia) progenitors. If such objects are indeed persistently X-ray luminous and embedded in sufficiently dense ISM, they will be surrounded by extended nebular emission. These nebulae should persist even long after a SN Ia explosion, due to the long recombination and cooling times involved. With this in mind, we searched for nebular [O III] emission around four SSSs and three SNRs in the Large Magellanic Cloud, using the 6.5m Baade telescope at Las Campanas Observatory and the IMACS camera. We confirm that, out of the four SSS candidates, only CAL 83 can be associated with an [O III] nebula. The [O III] luminosity for the other objects are constrained to $\lesssim 17$ per cent of that of CAL 83 at 6.8 pc from the central source. Models computed with the photoionization code CLOUDY indicate that either the ISM densities in the environments of CAL 87, RX J0550.0-7151 and RX J0513.9-6951 must be significantly lower than surrounding CAL 83, or the average X-ray luminosities of these sources over the last $\lesssim 10,000$ years must be significantly lower than presently observed, in order to be consistent with the observed luminosity upper limits. For the three SNRs we consider (all with ages < 1000 years), our [O III] flux measurements together with the known surrounding ISM densities strongly constrain the ionizing luminosity of their progenitors in the last several thousand years, independent of the progenitor channel.

Key words: supernovae: general – ISM: supernovae remnants – binaries: close

1 INTRODUCTION

For many decades the origin of Type Ia supernovae (SNe Ia) has remained elusive. Early proposals of the explosion of a white dwarf close to the Chandrasekhar mass (Hoyle & Fowler 1960) were theoretically confirmed as early as the 1970s (Wheeler & Hansen 1971; Nomoto et al. 1976) and the subsequent progress in both modelling and computing power has allowed for an ever-improving match between theory and observation (Blondin et al. 2011; Moll et al. 2014; Raskin et al. 2014; Polin et al. 2019). Presently, it is understood that a SN Ia is an exploding white dwarf (see Livio & Mazzali 2018, for a recent review). The strength of this scenario in explaining the standardizable energy output of SNe Ia, which led Kowal (1968) to highlight their potential as cosmological distance indicators, was exploited to great success with the discovery of Cosmic Acceleration (Riess et al. 1998; Perlmutter et al. 1999).

There remains considerable contention, however, in understanding why a white dwarf should explode as a SN Ia. In the classic model (Wheeler & Hansen 1971), a massive white dwarf accretes matter from an interacting binary companion until triggering an explosion (the Single Degenerate Scenario, SD); alternatively, Iben & Tutukov (1984) and Webbink (1984) presented the merging of two white dwarfs as another pathway to explosion (known as the Double Degenerate scenario, DD). A number of variations on these two pictures have since emerged (e.g., Rosswog et al. 2009; Di Stefano et al. 2011; Kashi & Soker 2011), however, we still do not know how a white dwarf may approach the catastrophic instability leading to its explosion as a SN Ia.

In recent years, both channels have alternatively received observational support and discouragement (for recent reviews of SN Ia progenitor models and observational constraints, see Livio & Mazzali 2018; Ruitter 2020). Challenging the classical single-degenerate scenario, there have been no observations of surviving companion stars

* E-mail: dnfarias@uc.cl (DNF)

associated with SNe Ia, i.e. near the location of a thermonuclear supernova remnant (hereafter SNR, [Edwards et al. 2012](#); [Schaefer & Pagnotta 2012](#); [Ruiz-Lapuente 2018](#)) and, in general, the lack of hydrogen in SN Ia spectra argue against a main sequence or giant donor consistent with the SD channel. DD channels largely satisfy these constraints (though may still yield surviving companions, see [Kerzendorf et al. 2018](#)), however the observed global symmetry of SN Ia explosions remains difficult to reconcile with this model ([Wang & Wheeler 2008](#)). Many approaches have been used to probe the nature of the progenitors of individual known SNe Ia: very early observations of SN 2011fe led to constraints on the size of the exploding star ([Nugent et al. 2011](#)), while pre-explosion images set strong upper limits on the luminosity of its possible SD ([Graur et al. 2014](#)) and DD progenitor systems ([Li et al. 2011](#)). The claimed discovery of the companion star of the SN 1572 (Tycho’s supernova, [Ruiz-Lapuente et al. 2004](#)) later proved controversial ([Kerzendorf et al. 2009](#)), and subsequent efforts to discover surviving companions have found no other candidates for Tycho or other SN Ia remnants ([Kerzendorf et al. 2018](#); [Ruiz-Lapuente 2018](#)).

Searching for evidence of persistent ionizing emission prior to explosion provides a particularly vital test of single degenerate models due to their frequent association with supersoft X-ray sources (SSS, [Kahabka et al. 1994](#); [Kahabka & van den Heuvel 1997](#)). These objects have extremely soft X-ray spectra, much softer than the classical X-ray binaries with neutron star or black hole accretors, and luminosities on the order of the Eddington limit ([Kahabka & van den Heuvel 1997](#)). To explain their unique spectra, [van den Heuvel et al. \(1992\)](#) were the first to propose that SSSs should be compact objects accreting hydrogen or helium rich material from a companion star at the same rate that it burns close to the surface; this regime is usually called the steady stable-burning-state (see [Sienkiewicz 1980](#); [Nomoto 1982](#), for hydrogen and helium accretion, respectively). When hydrogen is accreted (at a specific rate $\dot{M} \sim 10^{-7} M_{\odot} \text{yr}^{-1}$) onto the envelope of the WD ($M_{\text{WD}} \approx 0.7 - 1.2 M_{\odot}$), it burns at a steady rate and emits significantly in the X-ray band as a blackbody with effective temperatures about 5×10^5 K. This rate is approximately that of thermal timescale mass-loss from a moderately evolved donor ([Nomoto et al. 2007](#)). The large flux of X-ray radiation resulting from the nuclear-burning at the surface of the WD (a few times 10^{37} erg s $^{-1}$) can ionize the interstellar medium (ISM) to distances of dozens of parsecs ([Rappaport et al. 1994](#)). Thus, ionized nebulae are expected to be associated with SSSs (also called ‘supersoft nebulae’).

As opposed to the method of directly detecting their X-ray emission, searching for supersoft nebulae has been suggested as a more efficient way to find SSSs, since the wavelength of typical nebular emission lines are much less affected by ISM absorption than the X-rays ([Rappaport et al. 1994](#); [Kahabka & van den Heuvel 1997](#)). For the Large Magellanic Cloud (LMC), in particular, the hydrogen column densities along the line of sight are in the range of 5×10^{20} to 3×10^{21} cm $^{-2}$ (see [Kuuttila et al. 2019](#); [Gänsicke et al. 1998](#)), which implies that the absorption due to the gas principally affects those X-rays with energies less than

0.5 keV. [Remillard et al. \(1995\)](#) did a search for supersoft nebulae surrounding SSSs in the LMC and found only one, CAL 83, out of nine that they observed. Two main hypotheses have been proposed to explain this ([Di Stefano et al. 1995](#)). One is that the luminosity of the SSSs varies in time, and that the average is lower than those inferred from the current X-rays observations. The other is that the surface brightness of the supersoft nebulae is below the thresholds of detection because the ISM around the sources has a very low density. Both studies tentatively conclude that roughly 10 per cent of supersoft sources would be associated with ionization nebulae, and that SSSs which are in the steady-burning state are likely to have surrounding nebulae. [Woods & Gilfanov \(2016\)](#) developed a statistical argument to conclude that most of the SSS nebulae in the LMC must lie in an ISM much less dense than that of CAL 83. Notably, for SN remnants, the expanding shock provides a natural probe of both the surrounding ambient ISM’s density and, in some cases, the neutral fraction, eliminating this ambiguity; this has previously been utilized by [Woods et al. \(2017\)](#) to exclude most accretion scenarios for the progenitor of Tycho’s supernova. By similar means, [Woods et al. \(2018\)](#) and [Kuuttila et al. \(2019\)](#) have set constraints on the luminosity of the progenitor of SN 1006, and several SN remnants in the LMC.

Our aim in this work is to find nebulae surrounding known SSSs in the LMC and relic nebulae surrounding recent SN remnants. Our motivation is twofold. On one hand, we want to revisit some of the fields studied by [Remillard et al. \(1995\)](#) using more modern instrumentation for observing and more developed software tools for the analysis. [Woods & Gilfanov \(2016\)](#) suggested that using 6–8m-class telescopes, and the same observing times of [Remillard et al. \(1995\)](#), much stricter upper limits on the [O III] $\lambda 5007$ Å surface brightness could be established, and that for typical SSS temperatures and luminosities, nebular densities could be constrained down to $n = 0.1$ cm $^{-3}$. This would mean a factor of four improvement over the upper limits established by [Remillard et al. \(1995\)](#). At the same time, we want to find relic nebulae surrounding young Type Ia supernovae remnants. The very long recombination times at the measured ambient ISM densities for these remnants support the hypothesis that, if a supersoft nebula existed before the explosion, it will remain there for many thousands of years, with the precise timescale depending on the particular optical emission line of interest. Overall, the H-recombination time of any putative photo-ionized nebula is of order $\tau_{\text{rec}} \approx 10^5 (n_{\text{ISM}}/1 \text{cm}^{-3})^{-1}$ yr ([Woods & Gilfanov 2016](#); [Woods et al. 2017](#)). For doubly-ionized oxygen, however, responsible for the strong, collisionally-excited forbidden line [O III] $\lambda 5007$ Å (an important coolant in such nebulae), the recombination timescale is:

$$\tau_{\text{O}^{2+}_{\text{rec}}} \sim 10^4 \left(\frac{n_{\text{ISM}}}{1 \text{cm}^{-3}} \right)^{-1} \text{yr.} \quad (1)$$

(see e.g., [Osterbrock & Ferland 2006](#)). Note here that the cooling time in such a nebula is similarly of order ten thousand years; together these timescales set the observable

lifetime for any nebula after the turn-off (or explosion) of its source. For any hot, luminous progenitor scenario, young SNe remnants such as those found in the LMC with ages ~ 500 yrs (Rest et al. 2005) would still be embedded in these associated nebulae long after the explosion. Finding supersoft nebulae around SSSs and recent Type Ia SN remnants would support the idea that the SSSs are indeed progenitors of SN Ia, and allow one to infer the effective temperatures and luminosities of the progenitors prior to explosion. An additional strength of observing the LMC is that its distance is well known (≈ 50 kpc, see Walker 2012, and references therein). This, together with a precise determination of the surrounding ambient ISM densities (e.g., Kosenko et al. 2010), ionization fractions (e.g., Ghavamian et al. 2000), and in some cases light echo spectra of the original supernovae (Rest et al. 2005), allows for a more certain translation between the apparent and intrinsic properties of the source and nebulae and a more precise connection between observations and models.

We took images of LMC SSSs and recent Type Ia SNRs in a narrow passband centered on the wavelength of the [O III] $\lambda 5007\text{\AA}$ transition at the redshift of the LMC and the standard V broadband (which contains this line). The subtraction of these images provides the flux emitted in the line without the contribution from the continuum. Modeling the measured emission with a photoionization code, we can set constraints on the properties of the nebulae and the SSSs. In §2 we describe the fields observed and in §3 we introduce our observations. In §4 we discuss the reduction and analysis methods and in §5 we present our results and compare them with simple theoretical models. Finally, in §6 and 7 we give a discussion and conclusions of our study.

2 TARGETED FIELDS

We selected four SSSs in the LMC, CAL 83, CAL 87, RX J0550.0-7151 and RX J0513.9-6951, as well as three SN remnants, SNR N103B, SNR 0519-69.0 and SNR 0509-67.5. The four SSSs were observed by Remillard et al. (1995), who detected an ionization nebula only in CAL 83. They measured a total [O III] luminosity of 1.26×10^{35} erg s $^{-1}$, integrated up to 7.5 pc from the source¹. For the other three sources, they set an upper limit on their bolometric luminosities $L \sim 10^{34.3}$ erg s $^{-1}$, more than a factor ten below the detection in CAL 83, so long as the density of the surrounding ISM is comparable to that in the vicinity of CAL 83. Higher luminosities, however, remained possible if the surrounding ISM density were lower, and indeed, CAL 83 is now understood to lie in an unusual over-density (see e.g., Woods & Gilfanov 2016, for further discussion).

Regarding the SNRs there is an ample consensus that they correspond to Type Ia SN explosions (Badenes et al. 2009) and no detection of [O III] regions around them has been reported. Kuuttila et al. (2019) studied the He II $\lambda 4686$ Å surface brightness profiles around these remnants (at ≈ 5 pc from the source) using IFU observations and put strong

upper limits (of order of 10^{-19} erg s $^{-1}$ cm $^{-2}$ arcsec $^{-2}$) in the He II emission line. Their method is similar to that used in this work, but here we focus on the much stronger [O III] 5007\AA line. Some additional information on the objects is given below.

2.1 CAL 83

CAL 83 was discovered in the original Einstein survey of the LMC (Long et al. 1981). It has been identified as a 17 mag variable blue stellar object and is the prototype of the SSS class with orbital period of 1.04 days (Hasinger 1994). The images of Remillard et al. (1995) show that the nebula is not symmetric around the source, and the brightness distribution indicate that it is not homogeneous. They do not give an intensity profile but report the integrated luminosities at two different distances (7.5 and 25 pc). They also report that there is a minimum of emission near the source, where surface brightness falls to ~ 50 per cent of the maximum.

Gruyters et al. (2012) did a spectroscopic study of a subregion of this nebula and, using the ratio of sulphur lines [S II] $\lambda 6716$ /[S II] $\lambda 6731$, estimated a mean electron density of $n \sim 10$ cm $^{-3}$. This is consistent with that quoted by Remillard et al. (1995) at 7.5 pc¹ from the source. The fact that the CAL 83 [O III] nebula is not spherically symmetric poses a challenge when modeling it.

2.2 CAL 87

CAL 87 was also discovered in the *Einstein* telescope's first survey (Long et al. 1981) and is roughly a factor of four fainter than CAL 83 (Hasinger 1994). It was identified with a binary star, in this case an eclipsing binary with an eclipse depth of 2 mag, mean V magnitude of ~ 19 and a period of 10.6 hours (Cowley et al. 1990). From observations, it has been suggested that we are seeing only the accretion disk since the WD should be more luminous. Absorption by the disk would reprocess the soft X-rays from the WD, and explain the missing radiation (Starrfield et al. 2004).

2.3 RX J0513.9-6951

This is the most luminous of the known SSSs in either the Milky Way or the Magellanic Clouds. Its X-ray variability was discovered during the ROSAT All Sky Survey (Schaeidt et al. 1993). Its binary companion was identified, with an orbital period of 0.76-days, from optical light curves (Hutchings et al. 2006). RX J0513.9-6951 displays some unusual characteristics such as repeated X-rays outbursts on timescales of years (Crampton et al. 1996).

2.4 RX J0550.0-7151

RX J0550.0-7151 was not detected by *Einstein* but was discovered by Cowley et al. (1993) as a bright and very soft source that lies only ~ 45 arc minutes SW of CAL 87, in the same ROSAT frame. It has been mentioned in fewer references than similar objects in the LMC, which mostly refer to its symbiotic nature. Schmidtke & Cowley

¹ Assuming a distance of 55 kpc to the LMC.

(1995) first noted that this is a symbiotic system and gave an improved position², which is nearly coincident with a fairly bright red star ($V = 13.53$, $B - V = 1.45$, $U - B = 0.86$). They, as well as Charles et al. (1996), verified the presence of Balmer emission lines superposed on the spectrum of a cool star, a characteristic feature of symbiotic stars³. The coordinates of this object (transformed to J2000.0 as they appear in the Catalog of Supersoft X-ray sources, SSSCAT⁴), are given in Table 1.

By 1996, Reinsch et al. (1996) found the source in an off state, and there have since been no further X-ray detections. Together with a failed radio detection (Fender et al. 1998)⁵, these later observations have cast some doubt on the nature of this object.

There is additional confusion regarding RX J0550.0-7151 because its name appears with slightly mismatching figures in different papers and surveys, likely originating in the difference between the coordinates at epochs 1950.0 and 2000.0. The name used by Fender et al. (1998) was RX J0550-71. SIMBAD associates this name with RX J0550.0-7151⁶. Reinsch et al. (1996) call it RX J0549.9-7151 and Kahabka et al. (2008), who additionally point out that the SSS does not have an optical counterpart, name it RX J0550.9-7151. More significantly, while previous works considered this SSS a symbiotic system, Schmidtke et al. (1999) pointed out that the observation of RX J0050.0-7151 (another mismatch) was blended with RX J0549.8-7150 and that subsequent analysis (H. C. Thomas, 1996, private communication) resolved the two sources⁷. This field was observed again with Chandra ACIS-S but the source was not detected (Orio et al. 2007).

2.5 SNR N103B

The young supernova remnant (SNR) N103B is the fourth brightest X-ray remnant in the LMC (van der Heyden et al. 2002), with a luminosity in the 0.15 – 4.5 keV band of 1.5×10^{37} erg s⁻¹ (Hughes et al. 1995). Its radial extent is about 3 pc. From its light echoes, Rest et al. (2005) estimated the age of N103B to be 860 yr and confirmed its nature as a SN Ia remnant from the light echo spectra. The latter has been questioned by Someya et al. (2014), who studied the ISM surrounding the remnant and found that the progenitor consisted of an hydrogen-dominated plasma, suggesting that the explosion should have been a Type II. Optically, N103B consists of small bright knots with emission-line spectra typical of SN remnants: [O III] λ 5007, [S II] λ 6716, 6731, H α (Hughes et al. 1995). Li et al. (2017)

has suggested that the star closest to the explosion centre may be a candidate companion for this SNR.

2.6 SNR 0519-69.0

Its radial size is 3.6 pc (Hughes et al. 1995). Its spectra is Balmer dominated indicating conditions of low excitation. Its age, from light echoes, is 600 ± 200 years (Rest et al. 2005).

The remnant was studied in X-rays by Hughes et al. (1995), the SNR is oxygen-poor and iron-rich better consistent with the result of a thermonuclear supernova (SN Ia) (Kosenko et al. 2010). Li et al. (2019) found a star that is a candidate to the companion star in the SD scenario, based on a peculiar radial velocity which deviates more than 2.5σ from the mean of the underlying stellar population.

2.7 SNR 0509-67.5

This is the youngest and most symmetric of the four LMC SNRs confirmed as SN Ia remnants (Edwards et al. 2012). It size is about 3.3 pc (Hughes et al. 1995), and Rest et al. (2005) set an age of 400 ± 50 years from the study of the light echoes. The spectra is also Balmer dominated. Since no companion has been found near the centre of the SNR (Schaefer & Pagnotta 2012), it was tentatively concluded that it is a result of a double degenerate channel, although the SN is spectroscopically classified as an overluminous SN Ia with light echoes (Rest et al. 2008).

3 OBSERVATIONS

Images at two epochs, December 12, 2015 and February 8, 2016, were taken with the Inamori Magellan Areal Camera and Spectrograph IMACS⁸ of the Magellan Baade Telescope at LCO, using the all-transmitting (all-spherical optics) f/4.3 long camera (known as the f/4 camera) for direct imaging. The f/4 camera, with eight mosaics of $2k \times 4k$ (MOSAIC3), observes a 15.4×15.4 arcmin field, which corresponds to a pixel scale of 0.111 arcsec per pixel. Two different filters were used for each observation: the Johnson-Cousins-Bessell V filter (5200 – 7750 Å) and a custom made narrow band filter centered at the observed wavelength of the [O III] 5007Å transition (see Figure 2). The transmission curves, in comparison with the Magellanic Clouds Emission Line Survey (MCELS) [O III]-filter and the Magellanic Cloud Photometric System (MCPS) Johnson B and V filter, can be seen in Figure 1. To remove the instrumental signatures, bias and flat-field images were taken at each observing epoch. A log of the observations is given in Table 1.

Unfortunately, both nights were non-photometric, with low density clouds streaming through the sky. This prevented us from obtaining an absolute calibrated photometry and further complicated the analysis.

Note that throughout this work we adopted the most

² RA₁₉₅₀: 5^h49^m46.7^s, DEC₁₉₅₀: -71°49′38″

³ For a review on the spectra of these objects see Kenyon & Webbink (1984).

⁴ <http://www.mpe.mpg.de/jcg/sss/ssscat.html>

⁵ Also, they do not obtained emission from CAL 83 and RX J0513.9-6951.

⁶ <http://simbad.u-strasbg.fr/simbad/sim-id?ident=RX+J0550.0-7151&submit=submit+id>

⁷ This remained a mystery because RX J0550.0-7151 faded below the detection level in the ROSAT All-Sky survey, 1995 data.

⁸ IMACS MANUAL.

Table 1. Summary of observations.

FIELD	(RA ₂₀₀₀ , DEC ₂₀₀₀)	t_{OIII} (sec) ^c	t_V (sec) ^d
CAL 83 ^a	(5 ^h 43 ^m 34.13 ^s , -68°22′21.9″) ¹	1200	300
CAL 87 ^{a,b}	(5 ^h 46 ^m 46.54 ^s , -71°08′53.9″) ²	1800, 1800	600, 300
RX J0513.9-6951 ^a	(5 ^h 13 ^m 50.8 ^s , -69°51′47″) ³	1800	600
RX J0550.0-7151 ^b	(5 ^h 50 ^m 0 ^s , -71°52′9″) ³	1800	180
SNR 0509-67.5 ^a	(5 ^h 09 ^m 31 ^s , 67°31′18″) ⁴	1200	210
SNR 0519-69.0 ^a	(5 ^h 19 ^m 35.14 ^s , -69°02′18″) ⁵	1200	300
SNR N103B ^a	(5 ^h 08 ^m 59.7 ^s , -68°43′35.5″) ⁶	1200	280

Taken in the ^afirst (12/12/2015) and ^bsecond (08/02/2016) epochs.

Approximated exposure time on ^c[O III] and ^dV Bessell filters.

¹ Gaia Collaboration (2018).

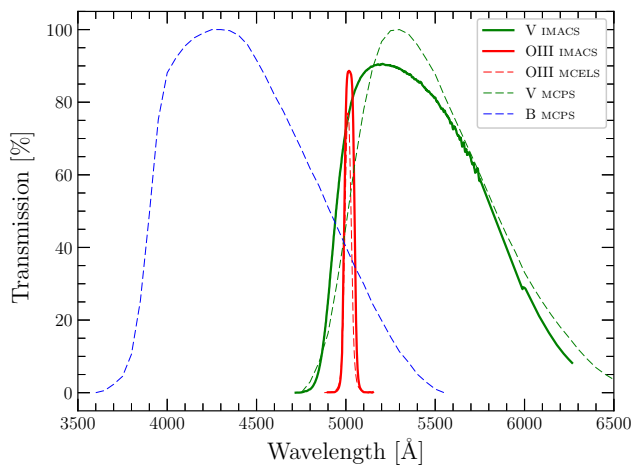
² Graczyk et al. (2011).

³ From SSSCAT.

⁴ Badenes et al. (2010).

⁵ Fuhrmeister & Schmitt (2003).

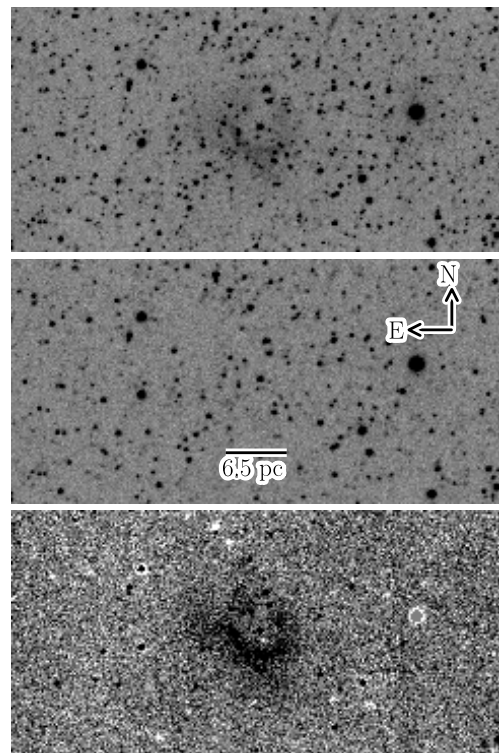
⁶ From Chandra Supernova Remnant Catalog.


Figure 1. IMACS Bessell V and [O III], MCELS O III and MCPS Johnson V filters.

up-to-date distance to the LMC, $D_{\text{LMC}} \approx 5 \times 10^4$ pc (Walker 2012). In order to compare the results with previous studies that used $D_{\text{LMC}} = 5.5 \times 10^4$ pc (e.g., Remillard et al. 1995; Rappaport et al. 1994; Gruyters et al. 2012), we corrected their projected distances in the LMC (e.g., 7.5 and 25 to 6.8 and 22.7 pc, respectively) and luminosities accordingly. With a pixel scale of $0.111''$, the projected distance in the LMC of one of our pixels is 0.026 pc.

4 REDUCTION AND ANALYSIS METHODS

The basic idea is to isolate the [O III] emission by subtracting a conveniently scaled V image from an [O III] narrow-filter image. This should provide the net [O III] emission of any potential ionized nebula surrounding a SSS or SNR. Prior to subtraction, the images must be appropriately processed.


Figure 2. From up to bottom, IMACS [O III], V and difference images containing the CAL 83 nebula. Dimensions of the images are $\approx 111'' \times 222''$.

4.1 Image Processing, alignment and subtraction

First, the images in both filters were corrected for bias and flat-field using calibration frames taken on the same observing runs and standard IRAF⁹ tasks. Then, since no

⁹ <http://ast.noao.edu/data/software>

WCS information was given in the raw images, ASTROMETRY.NET¹⁰ (Lang et al. 2010) was used to generate precise WCS information from scratch. The astrometrically aligned images were then fed to the differential photometry code PHOTPIPE, a pipeline created by Armin Rest and collaborators (see Rest et al. 2014, and references therein). We used PHOTPIPE to resample the images of each field in both filters to a common centre in order to align them in a pixel-wise sense. With the images aligned we subtracted the V passband from the [O III] image using HOTPANTS¹¹ (Becker 2015), the so called difference images. The ideal expected output is an image of the field where all the normal stars, together with any thermal continuum emission, have disappeared and the diffuse [O III] λ 5007Å emission of any putative nebula is highlighted. We found that, as long as the fields are not overly crowded with stars, the subtraction tends to produce reasonable results.

4.2 Photometric calibration

The next step is to find the relation between the counts in the difference image and the received flux in physical units, i.e., the photometric calibration. We derive it from the definition of count rate cps (typically in units of ADU s⁻¹), of a reference star with spectrum f_λ (in units of erg s⁻¹ cm⁻² Å⁻¹), measured under a certain filter X , as

$$\text{cps}_X = \int_X f_\lambda(\lambda) S_X(\lambda) d\lambda, \quad (2)$$

where $S_X(\lambda) = T_X(\lambda) \cdot T_{\text{atm},X}(\lambda) \cdot R(\lambda)$ is a generalized filter function including the transmission of the atmosphere ($T_{\text{atm},X}$, unitless), the optics (R_X , typically in units of ADU erg cm²) and the passband X (T_X , unitless, Spector et al. 2012).

In this case, the wide (W) and narrow (N) filters are the standard IMACS Bessell V and our custom made [O III], respectively. The measured “cps” values are formed by the contribution of the continuum (*cont*) and the emission line (*line*), as follows

$$\begin{aligned} \text{cps}_N &= \text{cps}_{N,\text{cont}} + \text{cps}_{N,\text{line}}, \\ \text{cps}_W &= \text{cps}_{W,\text{cont}} + \text{cps}_{W,\text{line}}. \end{aligned} \quad (3)$$

We follow Bessell & Murphy (2012) and assume that the width of the emission line is much narrower than the effective width of both [O III] (Δ_O) and V (Δ_V) filters (62 Å and 865 Å, respectively). If so, the flux of the line can be approximated by

$$\begin{aligned} f_{\text{line}} &\cong \frac{\text{cps}_{N,\text{line}}}{S_N(\text{line})} \\ &\approx \frac{\text{cps}_{N,\text{line}}}{T_N(\lambda_{\text{line}}) T_{\text{atm},N}(\lambda_{\text{line}}) R(\lambda_{\text{line}})} \\ &\approx \underbrace{\left\{ \frac{\text{cps}_N - \text{cps}_{N,\text{cont}}}{T_N(\lambda_{\text{line}})} \right\}}_{\Delta \text{cps}_N} \underbrace{\left(\frac{1}{T_{\text{atm},N}(\lambda_{\text{line}}) R(\lambda_{\text{line}})} \right)}_{\eta_N^{-1}}. \end{aligned} \quad (4)$$

The first factor in the last expression of Equation 4, Δcps_N , can be obtained directly from the image subtraction (we will further assume that $T_N(\lambda_{\text{line}}) \approx 1$). The second factor in this equation, η_N^{-1} , is the constant that must be found to accomplish the photometric calibration. Several observations of spectrophotometric stars at different airmass (or at similar atmospheric conditions) are needed to do so. The main problem with this, ideal, procedure is that there are no IMACS [O III] standard stars available so far and, hence, a calibration in the style of Spector et al. (2012) cannot be done.

On the other hand, the IMACS Bessell V filter is a standard passband, so its zeropoint can be approximately characterized by, for example, the Johnson filters used in the Magellanic Cloud Photometric Survey (MCPS¹²) for the catalog of objects in the LMC (Zaritsky et al. 2004), with magnitudes placed in the Johnson-Kron-Cousins system (Landolt 1992). Therefore, Johnson U , B and V magnitudes are available for the stars in each field.

Assuming that the (unavailable) IMACS magnitudes of the stars in each field are equal to the MCPS counterpart, m_* , for IMACS/MCPS V filter and that the Vega magnitude are $B = 0$, $V = 0.03$, the Vega calibrated magnitudes can be written as a function of the counts as follows,

$$m_* - m_{\text{VEGA}} = -2.5 \log \langle f_* \rangle + 2.5 \log \langle f_{\text{VEGA}} \rangle, \quad (5)$$

(Bohlin & Landolt 2015), where $*$ stands for either B or V , $\langle f_* \rangle \approx \text{cps}_V \cdot \Delta_V^{-1} \cdot \eta_V^{-1}$ and f_{VEGA} corresponds to the spectrum of Vega¹³.

Since we do not have useful spectra for any of the stars in the fields, we need to take a further step. Following the ideas underlying SED reconstruction (Brown et al. 2016), we assume that

$$\int_X f_\lambda S_X d\lambda \approx f(\lambda_{X,\text{eff}}) \cdot \Delta_X \cdot \eta_X \quad (6)$$

where $\lambda_{X,\text{eff}}$ is the effective wavelength of the filter X , defined as $\int T_X f_* \lambda d\lambda / \int T_X f_* d\lambda$, and $f(\lambda_{X,\text{eff}})$ is the flux of the star evaluated at this wavelength. In other words, Equation 6 indicates that the mean flux of an object under a filter, characterized by its effective width and wavelength¹⁴ can be approximated by the flux of that object evaluated in the effective wavelength.

Using Equation 5 for the B and V filters, leads to

$$\begin{aligned} f_*(\lambda_{V,\text{eff}} = 5435.5 \text{ \AA}) &\approx \langle f_{\text{VEGA}} \rangle_V 10^{-0.4 V_*}, \\ f_*(\lambda_{B,\text{eff}} = 4392.5 \text{ \AA}) &\approx \langle f_{\text{VEGA}} \rangle_B 10^{-0.4 B_*}, \end{aligned} \quad (7)$$

for $\Delta_B = 1009 \text{ \AA}$ and $\Delta_V = 864.7 \text{ \AA}$. Now, for each star,

¹² MCPS filters.

¹³ <ftp://ftp.stsci.edu/cdbs/calspec/>

¹⁴ With the caution that λ_{eff} is not perfect characterization of a filter because it depends on f_* (Bessell & Murphy 2012).

¹⁰ <https://github.com/dstndstn/astrometry.net>

¹¹ <https://github.com/acbecker/hotpants>

$f(\lambda_{\text{Oeff}} = 5019.4 \text{ \AA})$ is obtained by a simple interpolation of the fluxes evaluated at $\{V_{\text{eff}}, B_{\text{eff}}\}$, as follows

$$f_*(\lambda_{\text{Oeff}}) \approx \left\{ \frac{\delta f_{*\{B, V\}_{\text{eff}}}}{\delta_{\{B, V\}_{\text{eff}}}} \right\} \times \delta_{\{B, O\}_{\text{eff}}} + f_*(\lambda_{B_{\text{eff}}}), \quad (8)$$

where $\delta_{\{X, Y\}} = \lambda_X - \lambda_Y$ and $\delta f_{*\{X, Y\}} = f_*(\lambda_X) - f_*(\lambda_Y)$. Therefore, using Equations 2, 6 and 8, η_{O}^{-1} is determined as

$$\eta_{\text{O}}^{-1} = \frac{f_*(\lambda_{\text{Oeff}}) \cdot \Delta_{\text{O}}}{\text{cps}_{\text{O}}}, \quad (9)$$

with η_{O}^{-1} in units of $\text{erg s}^{-1} \text{ cm}^2 \text{ ADU}$. The time dependency of this equation is ignored since the flux in the difference image is measured in the same scale as the original [O III] image. In order to fit simultaneously all of the stars in the field, we used SCIPY Orthogonal Distance Regression (ODR)¹⁵ including the magnitude errors from the catalog. η_{O}^{-1} is our photometric zeropoint (Z_{F}).

The calibration procedure adopted above has been extensively detailed by Waller (1990). One relevant assumption of the method is that the effective wavelengths of both filters should be close to the wavelength of the line of interest. This is not well satisfied in our case, where the wavelength difference is $\sim 400 \text{ \AA}$. As a result, the approximated continuum contribution in Equation 4, $\text{cps}_{\{\text{N, cont}\}}$, will not be as well approximated by cps_{V} as could be, and calibration of the subtraction will be more uncertain than desired. Remillard et al. (1995) alleviated this problem using a broadband image which was a combination of B and V images, whose effective wavelength lies much closer to the [O III] line. Cloudy weather in our two runs prevented us from collecting the necessary B images. The preference to calibrate and normalize by [O III], although more cumbersome for the lack of calibrated stars in the field, follows the historical approach.

4.3 Flux measurement

With the counts in the difference images calibrated, the next step is the construction and analysis of the SEGMENTATION images to determine what is diffuse emission in them. In essence, this is a simultaneous determination of what is background, what is noise and what is emission. The inputs are the image difference provided by HOTPANTS and the mask image provided by PHOTPIPE. The mask image removes pixels with higher noise resulting from the subtraction of bright stars, for example, although some marginal residuals are left. After experimenting with our data, we found that a useful additional sanity step is to reject pixels outside of the range $-100 \leq \Delta_{\text{cps}} \leq 100$, which are clearly unrelated with real emission.

We then go through a two step iteration combing the resulting masked difference image with the routine DETECT_SOURCES from the PYTHON package PHOTUTILS DETECTION¹⁶, which requires three additional parameters

to define an emission region: a signal threshold, a minimum number of neighbouring pixels, $npixels$, with signal above this threshold, and a connectivity number. The latter parametrizes the grouping condition, set to require either four-connected pixels touching along their edges, or eight-connected pixels touching along their edges and corners. After some experimentation, we found that $npixels=20$ was a good value for our images because it allows us to reject any residual from subtraction of bright stars left by the mask and previous filtering, since their total areas are composed of ~ 20 pixels at most (this, in turn, is related with the fact that the typical FWHM in our images is about 10 pixels). A larger value of $npixels$ may more robustly reject this noise, but is not desirable because this would also reject real emission from the nebula. Connectivity proved to have a marginal effect, and we decided to set it to the less restrictive value of four.

Setting the threshold for detection requires particular care. In principle, this is provided by the statistics of HOTPANTS through the parameters MEAN PIX and STD PIX. Basically, MEAN PIX is the mean of the pixels that were used in the calculation of the kernel to differentiate the images, while STD PIX is the standard deviation of those pixels. These values essentially define the background and have a direct impact in what we will later determine to be net emission from the nebula. We determine this in an iterative manner. First, we do an initial pass through DETECT_SOURCES using a threshold of one HOTPANTS standard deviation (one STD PIX), in order to select pixels that have even a small chance of being emission, calling the remaining pixels as “background”. Then, we create a smoothed background image by fitting a linear surface to those pixels (i.e., adjusting functions of the form $Ax + By + C$)¹⁷. Assuming then that this background is sufficiently accurate, we subtract it from the image, recompute the mean value and standard deviation, and redo the DETECT_SOURCES step, but now using the much more stringent requirement of five standard deviations to reject a pixel. The means and standard deviations values of the smoothed backgrounds fitted resulted in $-1.5 \lesssim \text{count} < 1.5$ and < 1.5 , respectively, for all cases. The values of HOTPANTS MEAN PIX and STD PIX for our images are collected in Table 2.

4.4 Radial Measurement

The final step is to measure the surface brightness (SB) profiles in each of the fields. With the zero points and uncertainties Z_{F} and ΔZ_{F} calculated in Subsection 4.2, the transformation to flux is accomplished by multiplying the counts in each pixel ‘i’, x_i by Z_{F} ,

$$\hat{x}_i = Z_{\text{F}} x_i. \quad (10)$$

Error propagation gives the uncertainty of each pixel in flux,

$$\Delta \hat{x}_i = Z_{\text{F}} \sqrt{x_i^2 \left(\frac{\Delta Z_{\text{F}}}{Z_{\text{F}}} \right)^2 + \Delta x_i^2}. \quad (11)$$

¹⁵ <https://docs.scipy.org/doc/scipy/reference/odr.html>.

¹⁶ <https://photutils.readthedocs.io/en/stable/detection.html>

¹⁷ Using code available from: <https://gist.github.com/amroamro/1db8d69b4b65e8bc66a6>.

We follow [Graur & Woods \(2019\)](#) in measuring [O III] surface brightness by doing aperture photometry in annuli centered on the source. We used PYTHON PHOTUTILS APERTURE package¹⁸, and a custom made code¹⁹. We place the center of the annulus in the object, mask it, and obtain the SB profile as an array of the total counts in each corona.

Our first measurements of SB presented us the surprising result that some of the annuli had a negative flux value. We believe this originates in small errors in the image processing that resulted in the subtraction of a background slightly larger than appropriate. Even when our backgrounds were very close to zero, small uncertainties could add up to make the total “measured” counts in annuli with little or null emission less than zero, a result that is clearly nonphysical. A simple solution to compensate for this systematic effect is to add a constant to the pixel counts to compensate for this suspected overestimation of the background. As a rough estimate, we take this constant as the minimum value of the SB profile at any distance between one and twenty five parsecs from the source (after removing the outliers). Since, in the real world, nothing prevents the annulus with the lowest flux from having a flux larger than zero, our solution implies that, in cases where our background might have been overestimated, our flux measurements will be lower limits to the real flux.

4.5 Comparison with models

To gain some physical insight on our measurements of SB profiles we use version 13.05 of the photoionization code CLOUDY²⁰ ([Ferland et al. 2013](#)). For a given incident spectrum, initial gas density, spherically symmetric density profile and uniform chemical composition, the code computes the radiative transfer through the gas cloud, solving the equations of statistical and thermal equilibrium, thus keeping track of the detailed balance equations for ion population levels. As a result, the ionization state of the gas and the population of the energy levels are obtained, allowing for a prediction of the emitted spectrum at different distances from the source ([Woods & Gilfanov 2016](#); [Woods et al. 2017, 2018](#)).

In practice, CLOUDY provides the emissivity $\epsilon(r)$ of the model nebula, in units of $\text{erg cm}^{-3} \text{s}^{-1}$. This emissivity is integrated along the line of sight l in order to obtain the surface brightness profile ([Woods & Gilfanov 2016](#); [Kuuttila et al. 2019](#)),

$$SB_i(r) = \int_l \frac{\epsilon(r)}{4\pi} dl, \quad (12)$$

¹⁸ <https://photutils.readthedocs.io/en/stable/aperture.html>

¹⁹ Loosely based on this [SB code](#).

²⁰ www.nublado.org

numerically, we recover equation A1 of [Pellegrini et al. \(2012\)](#),

$$S_i = 2.3504 \cdot 10^{-11} \times \frac{1}{4\pi} \sum_k dl_k(x, y) \cdot \epsilon_i(x, y, z) \quad (13)$$

where S_i is now in units of $\text{erg s}^{-1} \text{cm}^{-2} \text{arcsec}^{-2}$, x , and y are such that $r^2 = x^2 + y^2$ (the distance from the source projected in the plane of the sky), and z and k describe the position of cloud elements perpendicular to the plane of the sky. The constant 2.3504×10^{-11} is the inverse of the number of square arcseconds that fit into one steradian.

The previous equations assume that the nebulae are spherical. This issue will be relevant when comparing observations and models because, as we will see, in the only case where we have a nebula to compare with (CAL 83, [Remillard et al. 1995](#)), there is no spherical symmetry.

We computed models assuming that the central source is a black body, and explored a large range of luminosities, $36 \leq \log L [\text{erg s}^{-1}] \leq 38$, and temperatures, $2 \leq T [10^5 \text{K}] \leq 7$, corresponding to the lower and upper limits used by [Woods & Gilfanov \(2016\)](#). We assumed that the ISM has an LMC-like chemical composition, with abundances one half the solar values, e.g., $[\text{Fe}/\text{H}] \sim -0.3$ dex ([Choudhury et al. 2018](#)), and took the neutral hydrogen density ranging from $-1 \leq \log n \leq 1$, in units of cm^{-3} .

We follow [Woods & Gilfanov \(2016\)](#) in setting the code-‘stopping’ condition at the distance where the temperature of the nebula falls below 3000 K. At these low nebular temperatures, the hydrogen ionization fraction falls below 10%, meaning that the ionization front is negligible. A thorough discussion on the usage of CLOUDY models, and the results that are obtained by this procedure, can be found in [Woods et al. \(2018\)](#).

5 RESULTS

We will present our results in three stages. We will first analyze visually the difference images to establish if there are systematic defects attributable to the software used, or unusual features in the fields that could bias the radial profiles to be computed later. Secondly we will describe the radial profiles computed for the different sources and compare them with independent measurements when they are available in the literature. We will then present our theoretical models for the profiles based on CLOUDY ([Ferland et al. 2013](#)) and finalize the section with a discussion.

5.1 Visual Inspection of Subtractions

This section is mainly based on the subtractions done with HOTPANTS. Table 2 presents some useful statistics provided directly by the code, such as the MEAN PIX and STD PIX, which are inputs of the first masking stage at SEGMENTATION. We note that CAL 87 2 and CAL 87 3 are the two different observations of this source, taken at different epochs, which fell on IMACS chip 2 and 3, respectively.

Table 2. Subtraction statistics for all of the fields: HOTPANTS MEAN PIX and STD PIX.

FIELD	MEAN PIX	STD PIX
CAL 83	1.711	6.611
CAL 87 2	-0.012	8.119
CAL 87 3	0.136	4.517
RX J0513.9-6951	1.822	12.046
RX J0550.0-7151	-0.171	4.958
SNR 0509-67.5	0.425	4.388
SNR 0519-69.0	3.734	11.596
SNR N103B	3.412	13.144

We see in Table 2 that SNR 0519-69.0 MEAN PIX is higher than that of CAL 83, where we already know there is emission. This could indicate that either the subtraction of this field was bad, with a large number of positive residuals of stars, or that there really is a large area of [O III] emission. The same can be said about SNR N103B and RX J0513.9-6951. All of these fields have large STD PIX values. No clear, relevant information regarding the other fields can be extracted from the table.

5.1.1 SSSs

We will start by analyzing the difference images of CAL 83, in particular the region shown in Figure 3 which spans a region of a $\approx 6.5 \times 6.5$ pc². This is an area of approximately $27'' \times 27''$ in the sky, which corresponds closely to the image size discussed by Gruyters et al. (2012).

These images are well suited to illustrate how the masking of bright objects works. The typical mask used in the DETECT_SOURCES task is smaller than required, i.e., some annular shaped residuals of star subtractions remained in the images, therefore it is necessary to enlarge these masks. To do this, we used the PYTHON BINARY DILATION routines.²¹ The dilation process primarily depends on the parameter ITERATION, which is the number of times that the code recursively dilates the mask. This presents a dilemma: few iterations leave bright rings around the masked objects, but too many iterations (e.g., ~ 30), results in large rhomboidal shaped masks at the position of the objects, rejecting from consideration the flux of possible emission pixels. After some trial and error, we converged on an ITERATION value of 10 as seen in the right panel of Figure 3. If we compare this image with the left panel, it can be seen that the residuals from stars are completely masked. For consistency, we used this value of ITERATION in all of the other fields. The masked pixel values are set to the mean of the calculated background in SEGMENTATION, which is always ≈ 0 .

In order to judge the quality of the subtraction, we show in the third panel of Figure 2 the combined [O III] (three images of 400 seconds) and the V image (image to be convolved in PHOTPIPE) covering the location of CAL 83 nebula.

The full size difference image of CAL 83, applying the

masks described above, is seen in Figure 4. This source is not embedded in a crowded field, which facilitates the subtraction and the masking. The nebula is located surrounding the source, as has been previously characterized by Remillard et al. (1995). The diffuse emission is clearly seen both to the NW of the source in Figure 3 and at the center of the image in Figure 4, as a yellow cross.

CAL 87 presents us with a different scenario. We took two images of this source, epoch 1 on chip 2 (Figure 5) and epoch 2 on chip 3 (Figure 6). The quality of the subtractions is not as good as that of CAL 83 because the field is more crowded. Small positive residuals at the positions of stars are abundant. These residuals are not masked by SEGMENTATION because they do not match the criteria of being an object with 20 or more connected pixels above the threshold. The comparison of the two independent images of CAL 87 presents us with a good case to understand systematic effects associated with the subtraction technique that will, eventually, appear as differences in the SB/FLUX profiles. We note that there is a discrepancy in their zero points, although they are consistent within the uncertainties. We will revisit this issue during the analysis of the radial profiles. Even though the statistics shown in Table 2 are computed from the unmasked HOTPANTS images, the results are consistent with the visual analysis. The MEAN PIX close to zero in CAL 87 difference images could not have been predicted just by looking at the masked version because of the prevalence of positive residuals of the stars. Therefore, it is clear that the masked objects are negative residuals in order to compensate what we are seeing. Nevertheless, the visual inspection indicates that neither of the difference images shows any kind of extended emission consistent with a nebula.

The difference image of RX J0550.0-7151, which was taken on epoch 2, is shown in Figure 7. It can be seen that it looks cleaner than those of CAL 87, with fewer masked objects. Again, no sign of extended emission surrounding the source, marked by a yellow cross, is seen. The MEAN PIX value is negative, but also the closest to zero of all the fields but CAL 87. This is consistent with the absence of positive residuals from stars after masking.

The last of the SSSs is RX J0513.9-6951 in Figure 8. The difference image is similar to that of CAL 87, with many residuals of stars and several masked stars. Although, in contrast to CAL 87, the large MEAN PIX value shown in Table 2 tell us that many masked stars were positive residuals.

Overall, the visual inspection of the difference images corresponding to SSSs leads us to the same conclusion of Remillard et al. (1995): There is no nebular [O III] emission detected surrounding them, with the only exception being CAL 83.

5.1.2 SNRs

The three SNRs in our sample show similar results. SNR 0509-67.5, shown in Figure 9, appears to be similar to CAL 87, both in the number of masked stars and the number

²¹ SCIPY BINARY DILATION

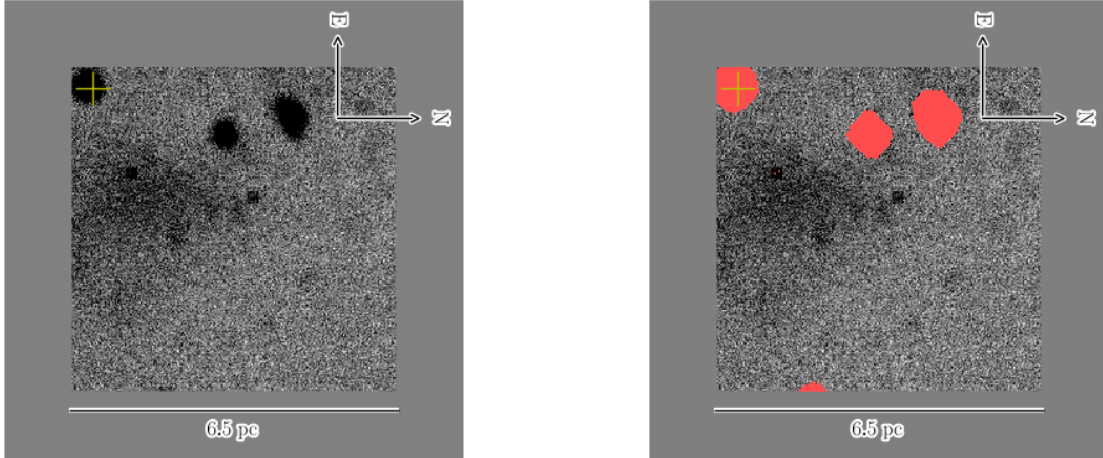


Figure 3. Difference images of a CAL 83 region near to the source. The left panel shows the image before masking and the right one after applying the masks in the SEGMENTATION stage (in red). The pixel values of the mask are ≈ 0 . Dimensions of the image are $\approx 6.5 \times 6.5$ pc², which makes the region shown approximately the same one studied by Gruyters et al. (2012). Diffuse emission is apparent to the eye centered at approximately 3 pc NW from the position of the source (yellow cross).

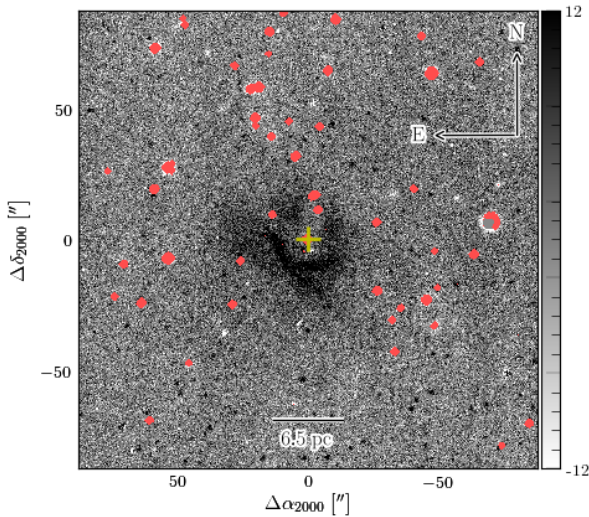


Figure 4. HOTPANTS difference image of CAL 83, and input of radial measurement, i.e., after masking the objects in SEGMENTATION. The small yellow cross is the approximated position of the source. The image is 1600×1600 pixels², which corresponds to $\approx 178'' \times 178''$.

and shape of the poorly subtracted stars. This fact, plus the MEAN PIX value registered in Table 2, suggests no emission at all.

SNR 0519-69.0, shown in Figure 10, is interesting. The large MEAN PIX value in Table 2 suggests, as in the case of CAL 83, that either there is some emission or the subtraction was very poor. Inspection of the difference image suggests that the latter is the most probable case. There is a large emission-like region in the left part of the image. What appears to be a circular object in the upper section is an instrumental artifact, probably related with a reflection in the [O III] filter that is not compensated by

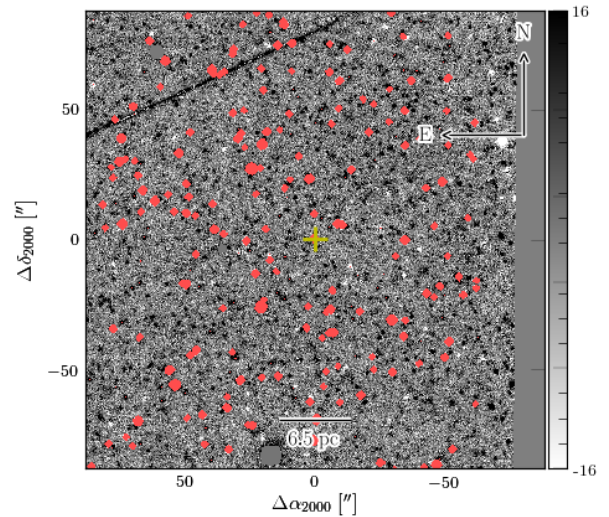


Figure 5. Masked HOTPANTS output of CAL 87 2, ready to be measured. There is no visible [O III] emission as CAL 83 nebula. Black straight line at NE is an artifact in the [O III] image.

flat-fielding (it is seen in other chips of the CCD array in some of the other fields). These structures increase the value of MEAN PIX accordingly. As for the rest, there are only masked pixels and residual stars surrounding the source, which also contribute to increasing the mean pixel value.

The last SNR of the set is SNR N103B, also known as SNR 0509-68.7, which is shown in Figure 11. This case shows a real detection of [O III] emission. First, the small-scale emission very close to center of the SNR is masked by the code, but a few small knots can be seen outside of the mask, near the location of the source marked by a yellow cross. These structures are well inside the outgoing shock of the remnant, and surrounded by many negative residuals

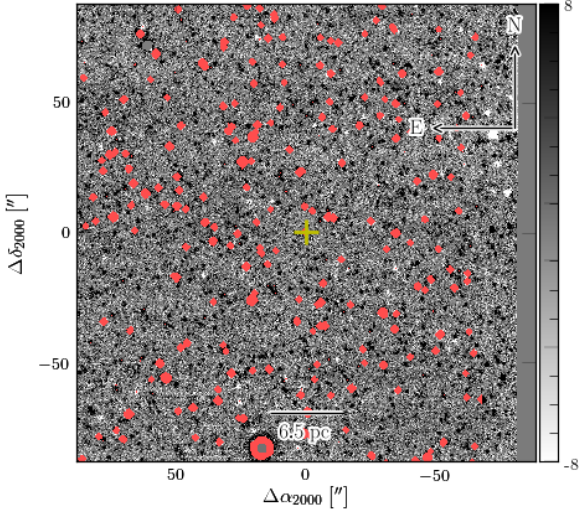


Figure 6. Same as Figure 5 but for CAL 87 chip 3. There is not much difference with its chip 2 counterpart. We expect that SB/FLUX profiles have similar shapes for this field, but different in scale due to the discrepancy in their corresponding Z_s .

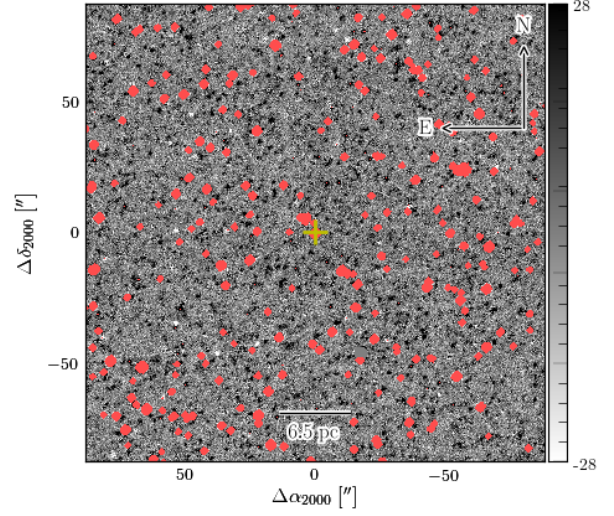


Figure 8. Same as previous difference images, for RX J0513.9-6951 field. It is remarkable the similitude between CAL 87 (Figures 5 and 6) and this image.

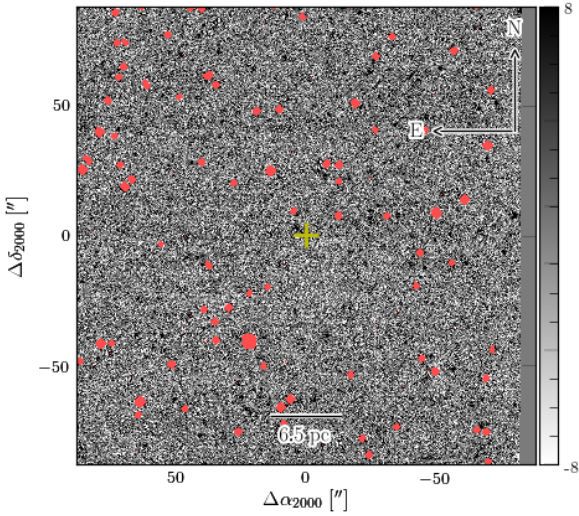


Figure 7. HOTPANTS RX J0550.0-7151 field image, after being mask in SEGMENTATION; visually, this subtraction looks cleaner than CAL 87, as there are not as many residuals, positive or negative, of stars, while the masked objects are few, such in the case of CAL 83.

from star subtractions. It is known that SNR N103B is a very complex structure (see Li et al. 2017, to appreciate all the physical structures of this SNR), but overall the local emission is overshadowed by that from an extended object seen towards the SW. This is a superbubble surrounding the stellar cluster NGC 1850²². Its contribution will certainly be noticed at $\approx 50'' \sim 12$ pc from the source.

²² <http://simbad.u-strasbg.fr/simbad/sim-id?Ident=NGC+1850>

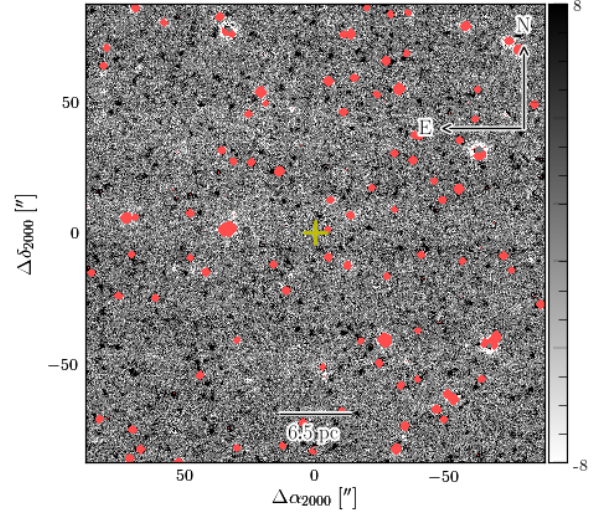


Figure 9. Difference image of SNR 0509-67.5; the resemblance with the (now prototype) CAL 87 counterpart is evident, which leads us to conclude that, at least visually, there is no [O III] emission from this field.

5.2 Emission profiles

We present here our measurements of [O III] emission radial profiles to be compared later with theoretical models. We estimate the energy summing total counts in annuli and using the conversion factor Z_F calculated as explained in Section 4.2. The values of Z_F and its uncertainty ΔZ_F for each source are given in Table 3. When measuring radially over the nebula, or suspected nebular region, we propagate the uncertainty ΔZ_F . In addition to the counts, it is necessary for constructing radial profiles to determine the distance from the source to each annulus. The position

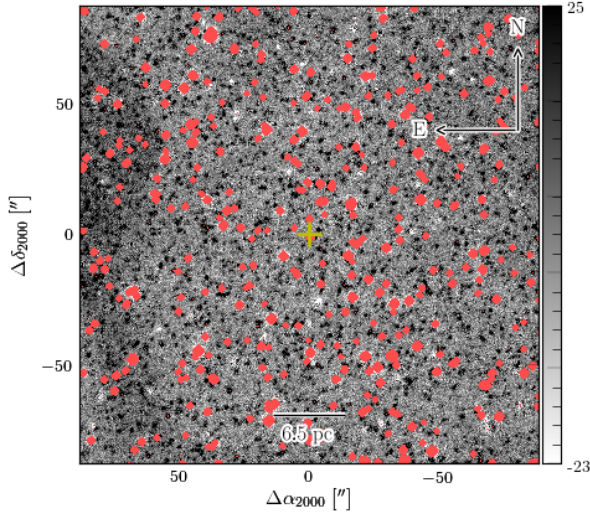


Figure 10. Difference image of SNR 0519-69.0 field. This is by far one of the most contaminated. See the details in Subsection 5.1.2.

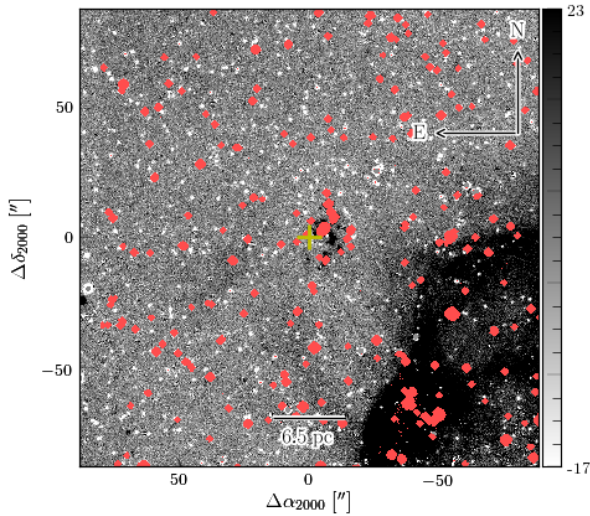


Figure 11. Difference image of SNR N103B. The complexity of the region is apparent. The superbubble is easily seen at SW. More details in Subsection 5.1.2.

of the sources are given in columns two and three in Table 1.

In the absence of a better option, we choose as pedestal the lowest mean value of the annuli. Table 4 provides the statistics for the annuli in all fields. MIN is the value of the pedestal subtracted. Most of the pedestals are consistent with zero, the exceptions being RX J0513.9-6951 and SNR N103B. The latter is by far the largest departure from zero of the list, but this is not surprising because its difference image indicates a problem with the subtraction, with many negative residuals on the stars surrounding the source, while the large emission region appears in the outskirts of the image. The pixels in this distant region add up

Table 3. Calculated Z_F and ΔZ_F in units of $\text{erg s}^{-1} \text{cm}^{-2} \text{COUNTS}^{-1}$.

FIELD	$Z_F \times 10^{19}$	$\Delta Z_F \times 10^{19}$	NUMBER OF STARS
CAL 83	2.022	0.458	773
CAL 87 2	1.017	0.246	1315
CAL 87 3	1.515	0.353	1367
RX J0513.9-6951	0.747	0.180	1062
RX J0550.0-7151	1.412	0.376	452
SNR 0509-67.5	1.407	0.332	612
SNR 0519-69.0	1.213	0.273	1414
SNR N103B	2.573	0.520	1684

Table 4. Corona statistics for all of the fields: minimum MIN, maximum MAX, mean MEAN and standard deviation STD.

FIELD	MIN	MAX	MEAN	STD
CAL 83	-0.252	10.199	1.751	2.497
CAL 87 2	-0.080	2.554	1.201	0.607
CAL 87 3	-0.280	1.445	0.688	0.336
RX J0513.9-6951	0.838	4.746	2.366	0.733
RX J0550.0-7151	-0.294	0.649	0.068	0.140
SNR 0509-67.5	-0.305	0.678	0.231	0.209
SNR 0519-69.0	0.041	5.337	2.422	1.476
SNR N103B	-2.504	6.108	2.317	2.550

to a larger positive value that compensates the negative isolated residuals, and therefore the field has a positive MEAN. Visual inspection clearly indicates the location of the MIN annulus and strongly suggests why it is negative. But the difficulty of masking the small residuals leads us to prefer using the pedestal instead of excising the individual residuals for a cleaner background subtraction.

Figure 13 displays the final SB profiles for the SSSs in our fields, while Figure 14 does for the SNRs, alongside some CLOUDY models (see subsection 5.3). For the fields with clear visual evidence of [O III] emission, the conclusions of our initial inspections in the previous section are confirmed: CAL 83, with a peak at ≈ 3 pc and a minimum at ≤ 1 pc from the source (given its doughnut shape), and the superbubble in the field of SNR N103B which contributes effectively from ≈ 10 pc. The rest of the sources do not show clear signs of emission. SNR 0519-69.0, the curious case that we named the worst subtraction of the list, shows an increment in the SB profile starting from ≈ 20 pc, which we associate with the instrumental artifacts discussed in the visual analysis. In any case, with the exception of CAL 83, none of the SNRs or SSSs show signs of an emission nebula around the source. This is consistent with the conclusions of the earlier work of Remillard et al. (1995) for the objects in common (i.e. the four SSSs).

Our results on the CAL 83 SSS nebula can be compared with those of the two previous studies examining it. Remillard et al. (1995) studied CAL 83, CAL 87, RX J0550.0-7151 and RX J0513.9-6951. For the former, they defined an inner region for the nebula extending up to

6.8 pc²³ from the source and indicated that, within it, the emission reaches a maximum at ~ 3 pc. They also commented that the region closer to 1 pc from the source represents a local minimum. Both of these observations are verified in this work, as seen in Figures 4 and 13. It is necessary to say that one of the observations made by Remillard et al. (1995) is not found in our profiles: they stated that, even if there is a local minimum close to 1 pc, it should be no less than 50 per cent of the intensity obtained at 3 pc; the reason for such a discrepancy is unclear but bears future study, but it is sure that masking and setting the values with the global mean must be taken into account. Remillard et al. (1995) also stated that the inner region contributes about 50 per cent of the total flux measured up to 22.7 pc. This amounts to $\sim 4 \times 10^{-13}$ and 8.2×10^{-13} erg s⁻¹ cm² respectively, neglecting the correction factor of 1.4 to account for Milky Way extinction (though they included this later when putting upper limits on the luminosity of the sources).

Finally, Remillard et al. (1995) set an upper limit to the luminosity of all of the other sources at 6.8 pc, the count rate of those sources is about a factor ten smaller than that of the CAL 83 inner nebula. They estimated that the total [O III] luminosity of CAL 83 at 22.7 pc was 3.4×10^{35} erg s⁻¹, corresponding to an upper limit of $\approx 10^{34.22}$ at 6.8 pc for the rest of the sources.

Our own measurements for CAL 83 are 0.91×10^{35} and 1.73×10^{35} erg s⁻¹ at 6.8 and 22.7 pc, respectively, using the same factor to correct for foreground extinction. Therefore, the upper limit of Remillard is about 17% of our measurement of CAL 83 at 6.8 pc (see Table 5) .

We can also compare with the results of Gruyters et al. (2012) who provide the only other published study of CAL 83 nebula. They used an IFU spectrum to study the flux emitted in about one quarter of the inner nebula, approximately the region displayed in Figure 3. A main conclusion of their work is that the total dereddened (reddened) [O III] flux in their quadrant is $\approx 9.7 \times 10^{-14}$ ($\approx 6.5 \times 10^{-14}$) erg s⁻¹ cm⁻². They state that the quadrant has dimensions of $25.5'' \times 25.5''$, or equal to 7.5×7.5 pc² at a distance to LMC of 55 kpc²⁴. Our measurement was done for an aperture of $27'' \times 27''$ (full FOV of their work), 6.5×6.5 pc² given the distance correction, centered to approximately match that of Gruyters et al. (2012), since they do not provide the centre for the aligned images.

Our result for this aperture is about $\approx 3.3 \times 10^{-14}$ erg s⁻¹ cm⁻² for masked data, a value smaller than the reddened value of Gruyters et al. (2012) (about 51% of their flux). If we compute the profile without applying any mask to the data (which considers several positive residuals), other than the one corresponding to HOTPANTS, and do not do background subtraction, the change of the total flux is about 37

²³ Originally, 7.5 pc in their work.

²⁴ There seems to be a mistake here. At 55 kpc $25.5'' \times 25.5''$ corresponds to $\approx 6.8 \times 6.8$ pc², while their full FoV is $27'' \times 27''$ (7.2×7.2 pc²).

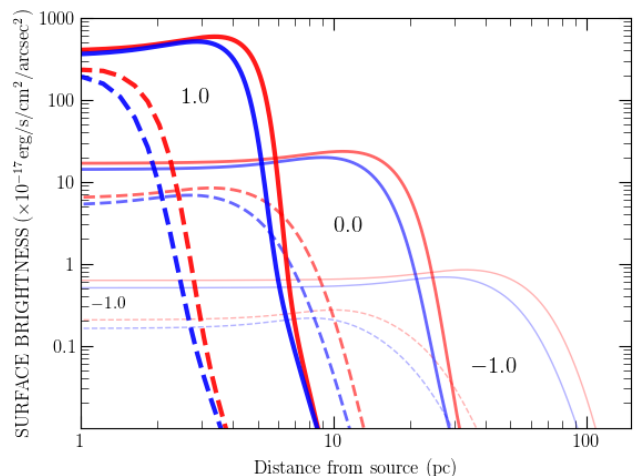


Figure 12. CLOUDY SB profiles for $\hat{n} \equiv \log_{10} n = \{-1, 0, 1\}$ (ISM density), $\hat{L} \equiv \log_{10} L = \{37, 38\}$ (luminosity of the source in dashed and solid lines, respectively) and $T_5 = T \times 10^{-5} = \{4, 5\}$ (temperature of the source in red and blue lines, respectively), with ranges of input parameters according to typical densities of ISM, and T, L of a SSS. These models were computed assuming LMC abundances (one half solar metallicity).

% larger (≈ 88 % the reddened value of Gruyters). Our measurements, hence, recover just a fraction of the flux of either Remillard et al. (1995) at 6.8 pc or Gruyters et al. (2012) closer to the source and appears to produce systematically low results.

5.3 Theoretical Modelling

We are now ready to compare the SB/FLUX radial profiles with CLOUDY theoretical models. The critical input parameters which we will vary throughout are the density of the ISM (n), and the temperature (T) and total luminosity (L) of the central source. The chemical composition, the other relevant parameter for CLOUDY models in this configuration, was fixed at one half solar abundance (typical of the LMC). Figure 12 illustrates the results of a study combining three ISM densities that span those expected for the LMC, with two radiation temperatures and two luminosities for the central source that span the characteristic range observed for SSSs. Curves in the figure are labeled by the values of $\hat{n} = \log n$, with n in units of cm⁻³, line-style coded according to the values of $\hat{L} = \log L$, with L in units of erg s⁻¹, and color coded according to the values of $T_5 = T \times 10^{-5}$, the radiation temperature of the source, with T in Kelvin.

Such models may be readily compared with our observations. We have plotted in Figure 13 all the empirical SB profiles of the SSSs obtained in Section 5.2, together with illustrative CLOUDY models computed for $\hat{L} = 37.5$ and $T_5 = 5$. All of the SSS SB profiles but CAL 83 are consistent with very low values of n , firmly excluding $n \gtrsim 1.0$ cm⁻³, and with many cases being consistent with the range $0.1 \lesssim n \lesssim 0.3$ cm⁻³. Comparing with the Figure 14, the SB profiles of all of the SNRs, we see that the only field with prominent [O III] emission like CAL 83 is the particular case

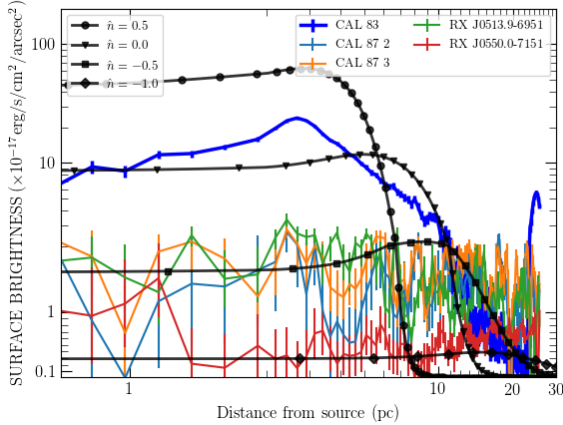


Figure 13. Empirical surface brightness profiles of all SSSs and CLOUDY models for $\hat{n} = \{-1.0, -0.5, 0.0, 0.5\}$, $\hat{L} = 37.5$ and $T_5 = 5$. The fact that only one profile, CAL 83, lies for sure above $n = 1 \text{ cm}^{-3}$ at mostly any distance from the central source, suggest that in normal conditions, there is no nebular emission surrounding the other sources. Otherwise, it would required a really low ISM density to explain these SB profiles in the figure, or a bad subtraction and/or flux calibration.

of SNR N103B. This is because at small distances from N103B, some emission from its unmasked knots remains while, at larger distances, it is difficult to separate any emission due to an hypothetical SSS fossil nebula from the contribution of the superbubble surrounding NGC 1850. Notice that the CLOUDY models of Figure 14 were calculated for the fixed values $\hat{L} = 37$ and $T_5 = 4$: as the most important parameter is the density, the conclusion of the SSS case remains, that for SNR 0509-67.5 and SNR 0519-69.0 the models that remain consistent are only those with $n \lesssim 1 \text{ cm}^{-3}$.

Taking the offset in flux measurement that we found in Section 5.2, between ≈ 1.2 and ≈ 2 , at face value, we could increase all the profiles by a factor between 20 percent and 100 per cent in order to account for possible error in our calibration. We would find, then, that almost all the fields would still fall below $n = 1 \text{ cm}^{-3}$. In the case of CAL 83, applying a factor two to the profile only just brings the observed profile into agreement with the $\hat{n} = 0.5$ model (that is, $n = 3.16 \text{ cm}^{-3}$ at 6.8 pc). This is marginally consistent with the lower bound of the interval $4\text{--}10 \text{ cm}^{-3}$ quoted by Remillard et al. (1995) and clearly smaller than the $\approx 10 \text{ cm}^{-3}$ given by Gruyters et al. (2012) (note however that the ISM in the immediate vicinity of CAL 83 is understood to be inhomogeneous, see Remillard et al. (1995) and Gruyters et al. (2012) for further discussion).

As we can see in Figure 12, some degeneracy exists between the n , L , and T input parameters. A higher luminosity model will be characterized by slightly more [O III] emission nearby the source and a generally more extended ionized region. In such a case, the CAL 83 profile is going to better represented by a model with a lower density than the previously obtained ($1 \lesssim n \lesssim 3 \text{ cm}^{-3}$), although this would be inconsistent with e.g., H α measurements (Remillard

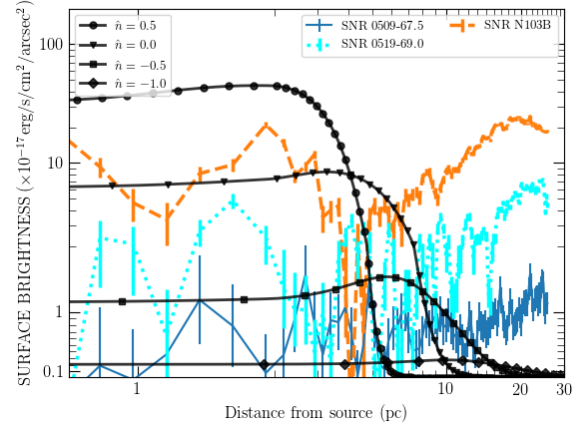


Figure 14. Same as Figure 13, but with the empirical models of our SNRs and models calculated for fixed values $\hat{L} = 37$ and $T_5 = 4$. In this case, we have more possibilities to explain the lack of emission for SNR 0509-67.5 and SNR 0519-69.0: 1) the ISM is too low, in concordance to the SSS case and 2) the time spent between the SSS phase and the SN explosion is comparable to the recombination time of the ISM.

et al. 1995), and may be excluded. The road to a source with higher luminosity seems to be closed, but that of lower luminosity sources appears to be possible. Decreasing the luminosity of the source and at the same time its radiation temperature, so as not to decrease the size of the ionized region, appears as an interesting option. With respect to the CLOUDY for $\hat{L} = 37$, $T_5 = 4$ in Figure 14, even if the SB profiles of no-emission fields are better constrained by $n \approx 0.3 \text{ cm}^{-3}$ CLOUDY model (i.e. a model than behaved as an upper limit before provides now a better match), the shape of the densest profiles provide a poorer match to the CAL 83 SB profile. In Figure 13, the profile $n = 1 \text{ cm}^{-3}$ provided a good qualitative fit to the observed SB profile, and approximately matched the extension of the nebulae. We can therefore conclude that $\hat{L} \approx 37.5$ is a better value for the time-averaged luminosity of a typical source, at least for a nebula like CAL 83.

Figure 15 presents a study of the FLUX enclosed in apertures of increasing size for CAL 83 compared with both CLOUDY models and the values $8.2 \times 10^{-13} \text{ erg s}^{-1} \text{ cm}^{-2}$ and $\approx 4 \times 10^{-13} \text{ erg s}^{-1} \text{ cm}^{-2}$, which are the measurements provided by Remillard et al. (1995) for the flux enclosed at 22.7 and 6.8 pc, respectively. The CLOUDY models of this figure were computed for a temperature $T_5 = 5$, luminosity $\hat{L} = 37.5$, and five different densities $\hat{n} = \{-1.0, -0.5, 0.0, 0.5, 1.0\}$. It is clear in the figure that $n = 1 \text{ cm}^{-3}$ provides the profile that better matches the observations, but that a value slightly larger would provide an even better match. On the other hand, the differences in shape between the empirical and model profiles probably indicate that the nebula does not have a constant density (see discussion above).

Figure 15 also sheds some light onto the mismatch

reported in Section 5.2 between the inner estimate of Remillard et al. (1995), consistent with that of Gruyters et al. (2012), and our own measurement. They reach the 50 per cent value given by the lower horizontal line at 6.8 pc and we do at ~ 20 pc. At 6.8 pc we are about 45 per cent below their estimate. Our measurement, however, is below theirs by 50 per cent at 22.7 pc. We are aware that the more precise flux in Remillard et al. (1995) is enclosed within the 22.7 pc aperture than the one within the 6.8 pc aperture²⁵ (Figure 15), we take the more conservative value at 6.8 pc, meaning that our calibration is underestimated by ~ 45 per cent. The differences, however, are within 3σ of the uncertainty in our zero point for this field at 6.8 pc (c.f. 3), as the σ deviations plotted in the Figure indicate. Gruyters et al. (2012) studied one quadrant of the CAL 83 nebula and provide a total [O III] flux of 6.52×10^{-14} erg s $^{-1}$, within 6.8 pc of the central source. We have plotted this measurement as well in Figure 15, assuming that the emission is spherically symmetric (although this is clearly only a crude approximation for CAL 83).

Our measurements, then, are consistent within the uncertainties with those of previous work. Since our relative flux calibration is more precise than our absolute flux calibration, the different discrepancies with Remillard et al. (1995) at different distances from the source indicate something more complex than just a difference of ~ 50 per cent in the zeropoints and the large masked zones.

Keeping in mind a possible uncertainty in flux calibration between our work and the previously reported measurements, and assuming that our zeropoints are consistent in all of our fields, we will measure the [O III] luminosity at 6.8 pc ($L_{\text{OIII},6.8}$), or their upper limit, for all our SSSs and SNRs and compare them with those resulting from CLOUDY models integrated to the same radius.

Figure 16 presents the results of this exercise. In order to simplify the analysis, and due to its smaller impact on the results, we use only one radiation temperature for the central source, $T_5 = 5$. We will allow four values for the luminosity, $\hat{L} = 36.5, 37.0, 37.5$, and 38.0 , which correspond to $\log(L/L_\odot) = 2.92, 3.42, 3.92$, and 4.42 , and allow the more critical parameter, the density of the nebula, to run between 0.1 and 10 cm^{-3} .

A look at the figure, and the summary of results in Table 5, confirms that our measurements of CAL 83 agree with those of previous studies. Our CLOUDY limits for central source luminosity $37.0 \lesssim \hat{L} \lesssim 37.5$ ($3.42 \lesssim \log L/L_\odot \lesssim 3.92$), leave a range of possible ISM densities for the nebula ($1.0 \lesssim n \lesssim 10 \text{ cm}^{-3}$), which is consistent with the range quoted by Remillard et al. (1995) and Gruyters et al. (2012) for their measurements within 6.8 pc ($1.0 \lesssim n \lesssim 10 \text{ cm}^{-3}$). For SNR N103B we do measure some emission, but we have already analyzed the case and concluded that it

²⁵ They write ‘The brighter inner nebula of CAL 83, which we measure by integrating the surface brightness out to a radius of 7.5 pc (6.8 pc) from the central object, contributes ~ 50 per cent of the total flux.’

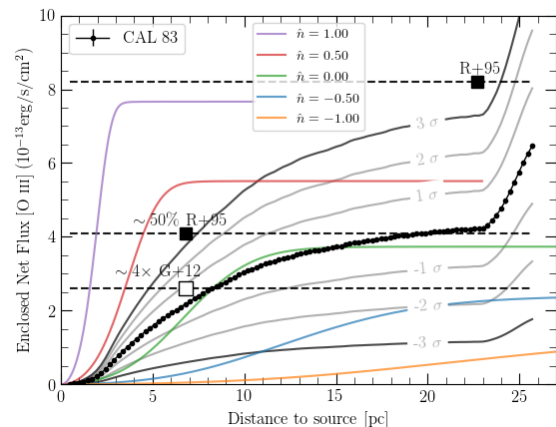


Figure 15. CAL 83 FLUX profile compared with the measurements of Remillard et al. (1995) & Gruyters et al. (2012) flux values at 6.8 pc and 22.7 pc from the source, and CLOUDY FLUX profiles, for $\hat{n} = \{-1.0, -0.5, 0.0, 0.5, 1.0\}$, $T_5 = 5$ and $\hat{L} = 37.5$. Our flux measurements are below those of Remillard et al. (1995) by ~ 45 per cent at 6.8 pc and ~ 50 per cent at 22.7 pc. The mismatch, though, is within 3σ of our uncertainty in the calibration for this field (c.f. 3). At 6.8 pc our value is about the same as that of Gruyters et al. (2012) (under the assumption of spherically symmetric emission).

is not emission associated with the kind of [O III]-emitting ionized region for which we are searching. For all of the other fields, we have nominal detections but, given the additional uncertainty in our calibration, we interpret these measurements as constraints on any extended nebular emission, all of which are more stringent than those of Remillard et al. (1995). As a result, only the assumption of extremely subluminous central sources, with time-averaged luminosities over their recent accretion history of $\hat{L} = 36.5$ or less, allows for densities of the surrounding nebulae comparable to that of CAL 83. Alternatively, for central source luminosities persistently comparable to that which is presently observed for these sources ($\hat{L} \gtrsim 37$), the required nebular densities are much lower, typical of either lower-density warm ISM or hot phase ISM. Factoring in the ~ 45 per cent difference with the flux of Remillard et al. (1995) does not substantially change the previous conclusion. Our upper limits in this case remain more stringent limits than those of Remillard et al. (1995).

In Figure 17, we similarly show our results for SNR 0509-67.5 and SNR 0519-69.0. Our limits on the progenitors of these SNe are obtained from searching for the minimum luminosity, at any distance larger than four and smaller than twenty parsecs from the source, of the model (in the bolometric luminosity-effective temperature grid) whose surface brightness profile exceeds the value of the observed surface brightness (we use a smoothed version of the latter to reduce the impact of the noise). For comparison, in the Hertzsprung-Russell diagram we have also plotted the accreting nuclear-burning WD models of Wolf et al. (2013) (black curves), alongside reliable ranges of the luminosity and temperature of the confirmed close-binary Magellanic

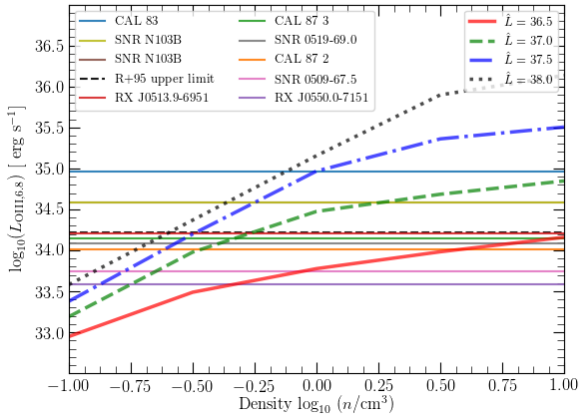


Figure 16. Logarithm of the [O III] luminosity, or its upper limit, enclosed within 6.8 pc of the central source ($L_{\text{OIII},6.8}$) for all the fields (see Table 5), together with the luminosity predicted by four CLOUDY models with $T_5 = 5$, four luminosities for the central source $\dot{L} = \{36.5, 37.0, 37.5, 38.0\}$ (corresponding to $\log(L/L_{\odot}) = 2.92, 3.42, 3.92, \text{ and } 4.42$), and nebular densities in the range of $-1.0 \leq \hat{n} \leq 1.0$. The upper limit to the luminosity of the nebulae undetected by Remillard et al. (1995), $\hat{L}_{\text{O}} = 34.3$, is also plotted.

Table 5. [O III] luminosity at 6.8 pc

Object	$L_{\text{OIII},6.8}^1$	Remarks
CAL 83	34.96	real nebula
SNR N103B	34.58	not a nebula
R+95 upper limit	34.22	upper limit
RX J0513.9-6951	34.20	nominal detection/upper limit
CAL 87 3	34.14	nominal detection/upper limit
SNR 0519-69.0	34.08	nominal detection/upper limit
CAL 87 2	34.01	nominal detection/upper limit
SNR 0509-67.5	33.75	nominal detection/upper limit
RX J0550.0-7151	33.58	nominal detection/upper limit

¹ Logarithm of the luminosity (erg s^{-1}) at 6.8 pc.

Table 6. Derived ISM densities around SSSs from the SB profiles.

Object ¹	$\log_{10} n$ (cm^{-3})
CAL 83	0.1
CAL 87 ²	< -0.1
RX J0513.9-6951	< -0.6

¹ No L_{bol} for RX J0550.0-7151.

² Both epochs.

SSS: 1. CAL 87; 2. 1E 0035.4-7230; 3. RX J0513.9-6951; and 4. CAL 83, in black boxes (Starrfield et al. 2004; Greiner 2000). It is easy to see the only source that lies in the permissible region of SNR 0509-67.5 is CAL 87, and this source is understood be observed edge-on, and may be more more intrinsically luminous (Starrfield et al. 2004). For SNR 0519-69.0, the case is different given that its upper limit is consistent with CAL 83 and 1E 0035.4-7230.

It is notable that the obtained upper limits are

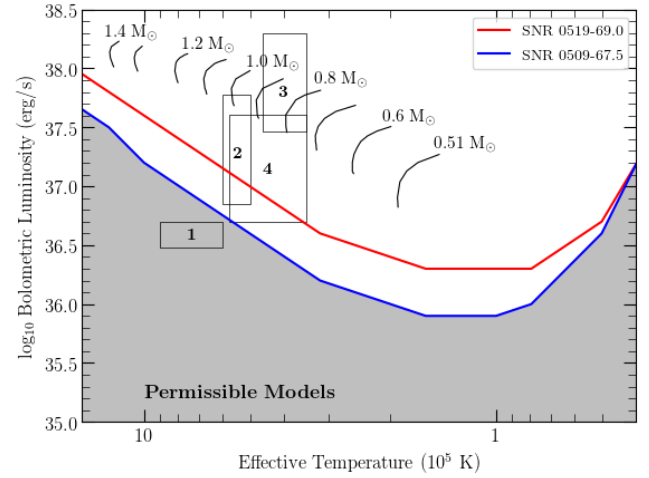


Figure 17. Measurements of the luminosity of SNR 0509-67.5 (red) and SNR 0519-69.0 (blue), for a given T (SNR N103B is excluded due to the uncertainty of the source of emission). Black curves are the accreting nuclear-burning WDs models from Wolf et al. (2013), while in black boxes are the estimated ranges of bolometric luminosity and effective temperature of the known close binary SSSs in the LMC: 1. CAL 87; 2. 1E 0035.4-7230; 3. RX J0513.9-6951; and 4. CAL 83 (Starrfield et al. 2004; Greiner 2000). The areas below each of the upper limits corresponds to the location of the permissible models for each source.

less stringent than the ones from Kuuttila et al. (2019) and Woods et al. (2018) (though independent), likely due to the aforementioned contamination in the difference images. The [O III]-derived upper limits for the progenitor of SNR 0509-67.5 are comparable to that obtained by Graur & Woods (2019) for the SN 2014J, using a similar approach.

Lastly, for CAL 83, CAL 87 and RX J0513.0-6951, the SSSs in our sample with known bolometric luminosities and effective temperatures, we have determined the model with the largest (surrounding) density whose SB profile exceeds the value of our smoothed observed SB, at any distance between one and twenty parsecs, assuming their presently-observed luminosities and effective temperatures have remained persistent over the last $\sim 10^4$ years, i.e., the O^{2+} recombination time in $0.1\text{--}1 \text{ cm}^{-3}$ gas. The results are shown in Table 6; it is readily apparent that if these sources are indeed persistent over long time scales, the ambient surrounding ISM densities inferred for CAL 87 and RX J0513.9-6951 are surely lower than for CAL 83, potentially indicating they are located well above the midplane of the LMC or in a region of hot ISM.

6 DISCUSSION

Our results are consistent with the earlier work of Remillard et al. (1995). The only detected [O III] emission nebula around a SSS is that of CAL 83. Although we manage to establish more sensitive upper limits, no [O III] ionized regions are detected with confidence around the other SSSs or SNRs. The exception, where some emission is measured, is SNR N103B. But, as discussed above, the

signal in this case does not correspond to a diffuse, fossil [O III] ionized nebula associated with the central source but to compact emission knots inside the expanding shock of the SN and a to a nearby superbubble (Williams et al. 2014).

One possible interpretation of the absence of other detected nebulae is that most SSSs undergo luminosity variations on much longer timescales than have presently been observed (\sim decades), in which they are primarily in the X-ray off state. Any variability that is shorter than a tenth of recombination timescale of hydrogen (recall Equation 1), should not strongly affect the ionization nebula SB profiles (Chiang & Rappaport 1996, though note that they do not investigate [O III] emission, but consider a constant-temperature nebula of H and He only). Given their presently observed duty cycles, the X-ray on (optically low) states of CAL 83 and RX J0513.9-6951 are \sim 200 and \sim 40 days, while the X-rays off states (optically high) are \sim 250 and \sim 140 days, respectively (Rajoelimanana et al. 2013). In these cases, then, detectable ionization nebulae are expected for both if the ISM density is sufficiently high. Therefore, either the time-averaged luminosity of RX J0513.9-6951 (and all of the other SSSs in the sample but CAL 83) is lower than the present value, i.e., there is a yet-unseen long term variability or long ‘duty cycles’, or e.g., the ISM surrounding them is much less dense than in the vicinity of CAL 83. The ‘duty cycle’ argument is also valid to explain the lack of emission in the SNR case, but notable for SNRs the densities are known.

Another possibility is the action of an optically thick wind reacting to accretion rates above the stable-burning region and obscuring the X-ray source (Hachisu et al. 1999), however this too should be observable, as the fast wind would excavate a cavity in the surrounding ISM and produce a dense expanding shell (see discussion in Woods & Gilfanov 2016). We are then led to conclude that either the ISM densities surrounding CAL 87, RX J0513.9-6951 and RX J0550.0-7151 are about \sim 0.1 cm^{-3} , or less, much lower than that of CAL 83, or that there is some other evolutionary process which obscures the soft X-ray emission of the sources and prevents the formation of the nebulae (see also Kuuttila et al. 2019, for further discussion).

The idea that the detection of ionized nebulae would help us to find an obscured SSS that cannot be detected via X-rays (Remillard et al. 1995), does not consider the possibility that the ionizing radiation could not reach the ISM around the source. The issue has been considered in studies trying to understand the discrepancy between the observed and expected number of SSSs in galaxies. We note Gilfanov & Bogdán (2010), who focus on elliptical galaxies, and Di Stefano (2010), who focus on spiral ones. Nielsen et al. (2013) proposed that the circumbinary stellar medium (CSM) surrounding a SSS should be able to obscure most of the radiation by the action of large mass loss from the system via a dense wind. This idea was rejected by Nielsen & Gilfanov (2015), who used CLOUDY to prove that these hypothetical nebulae would look very different from the expected SSS nebulae (Rappaport et al. 1994), with higher He II/H β and lower [O III]/H β ratios, while requiring mass loss rates comparable to the stable-burning accretion

rate ($\sim 10^{-7} - 10^{-6} M_{\odot}$) for a typical SSS system²⁶. The amounts of CSM material implied by this scenario would imprint features in the early spectrum of a SN Ia, which are very seldom seen (see Patat et al. 2007, for the case of SN 2006X). In particular, the lack of X-ray and radio detections from early observations of SNe Ia strongly constrains the mass loss rate from their progenitor systems, typically excluding symbiotic stars and even fast optically-thick winds (e.g., Chomiuk et al. 2016; Lundqvist et al. 2020).

With respect to the SNRs, our results are consistent with those of Kuuttila et al. (2019), although they use a different approach. They measured the surface brightness upper limits from the spectrum of the three SNRs, SNR 0509-67.5, SNR 0519-69.0 and SNR 0509-68.7, using the He II λ 4686 Å emission line from spectra taken at $\sim 4 - 5$ pc from the central sources. They did not find emission in any of the SNRs, and from the upper limit of He II emission of SNR 0519-69.0, and the constraints on the companion luminosity given by Edwards et al. (2012), they ruled out any possibility of a single degenerate progenitor, including SSSs. For SNR 0509-67.5, our results also agree with Woods et al. (2018) who have independently excluded the possibility of a SSS progenitor given the high content of neutral hydrogen in the surrounding environment. Note that Kuuttila et al. (2019) also discussed the possibility of constraining SNR progenitor luminosities by setting upper limits to the [O III] emission, in particular noting the [O III] λ 5007 line visible in the spectrum of SNR 0519-69.0 as an example. However, they noted the forward shock itself would contribute some UV-soft and X-ray radiation and this makes it necessary to model the whole SNR spectrum in order to separate a hypothetical relic nebulae in the immediate vicinity of the shock from the diffuse emission resulting from the ejecta. We avoid this ambiguity 1) by observing well beyond the shock front, and 2) because we claim only upper limits on a pre-existing fossil nebula (whereas a detection of such a nebula would require much more sophisticated modeling in order to distangle the shock-induced emission from the fossil nebula).

7 CONCLUSIONS

Although we are within 3σ of the results in the literature, the uncertainty in flux calibration prevents us from making a firm conclusion regarding the flux of any putative very low surface brightness nebulae for the sources in our sample (other than CAL 83). Practically speaking, going deeper using our present method would require background determination for our image subtraction to be accurate to within a fraction of an ADU across the whole field of view, and the difference between our measurements and those of Remillard et al. (1995) amounts to just $\lesssim 1$ ADU per pixel (2σ at 6.8 pc, exceeding literature value at 22.7 pc), without considering a better replacement of the masked values, notably near the source (see Figure 15). Particularly, we are concerned about the statistics provided by HOTPANTS when subtracting images taken with different filters, since

²⁶ $kT_{\text{eff}} = 50\text{eV}$, $L_{\text{bol}} = 10^{38} \text{ erg s}^{-1}$, inner/outer radial distances to the compact source $r_{\text{inn}} = 1 \text{ AU}$, $r_{\text{out}} = 10 \text{ AU}$, and wind speed $u_w = 10 \text{ km/s}$.

even in the optimal cases we tried, such as the subtraction between $V - V$ and $O - O$ filters of consecutive images, the results were puzzling to us.

Qualitatively, however, our results are fully aligned with those of previous works. Neither the SSSs (aside from CAL 83) nor the SNRs yielded a new detection of an [O III]-luminous ionized nebula. In addition, we have obtained the following new results:

(i) We have presented SB profiles around seven hot and luminous sources in the LMC, four SSSs and three SNRs. Notably, although CAL 83 was first studied in detail in 1995, our SB profile is to our knowledge the first published.

(ii) The [O III] flux measurement of the CAL 83 nebula at 6.8 pc is broadly (3σ) consistent with those in the literature. They reported a 50 per cent increase in luminosity between 6.8 and 22.7 pc and we measure about a 50 per cent increase, approximately, between the same radii, although reduced by a factor of two.

(iii) The shape of the [O III] SB profile is only crudely approximated by constant density CLOUDY models, consistent with previous studies which have determined that the ISM density in the nebula is not constant. The density of the ISM for CAL 83 at 6.8 pc is $\geq 1 \text{ cm}^{-3}$ for a persistent blackbody temperature of $T = 5 \times 10^5 \text{ K}$ and a luminosity of $L \leq 10^{37.5} \text{ erg/s}$, as observed for the source. This is consistent with the calculations by Gruyters et al. (2012, $\approx 4 - 10 \text{ cm}^{-3}$ for the inner nebula) using the values for the density, luminosity and temperature of the photoionized models from Rappaport et al. (1994).

(iv) The [O III] luminosities at 6.8 pc for almost all the fields are below $10^{34.2} \text{ erg s}^{-1}$, which is about 17 per cent of our measurement of the luminosity of the CAL 83 nebula.

(v) For the SSSs, the negative detections require either a much lower density ISM compared with that of CAL 83 (for CAL 87, $\lesssim 0.8 \text{ cm}^{-3}$; for RX J0513.9-6951, $\lesssim 0.25 \text{ cm}^{-3}$), or a very low ionizing luminosity averaged over the last \sim recombination timescale compared to their currently observed state. This is the first time such non-detections have been used to place a strong upper bound on the ISM density in the vicinity of CAL 87 and RX J0513.9-6951, providing a unique probe of the warm diffuse ionized medium in the LMC under the assumption that the presently observed SSS spectra are typical of at least the last several thousand years.

(vi) For the SNRs, the expanding remnant itself provides an independent probe of the surrounding ISM density; for this reason, we may unambiguously exclude any persistently hot and luminous progenitor within the last $\sim 10,000$ years. This result is consistent with other independent means of constraining their progenitors, (e.g., Woods et al. 2018; Kunttila et al. 2019; Graur & Woods 2019).

ACKNOWLEDGEMENTS

We thank the referee for their kind and insightful comments, which greatly improved the manuscript. This paper includes data gathered with the 6.5 m Magellan Telescopes located at Las Campanas Observatory, Chile. This research has made use of NASA's Astrophysics Data System. Support for DNF and AC was provided by ANID, through the Millennium Science Initiative grant ICN12-009 (MAS), and from grant

Basal CATA PFB 06/09. TEW acknowledges support from the NRC-Canada Plaskett fellowship.

DATA AVAILABILITY

The data underlying this article will be shared on reasonable request to the corresponding author.

REFERENCES

- Badenes C., Harris J., Zaritsky D., Prieto J. L., 2009, *ApJ*, **700**, 727
- Badenes C., Maoz D., Draine B. T., 2010, *MNRAS*, **407**, 1301
- Becker A., 2015, HOTPANTS: High Order Transform of PSF ANd Template Subtraction (ascl:1504.004)
- Bessell M., Murphy S., 2012, *PASP*, **124**, 140
- Blondin S., Kasen D., Röpke F. K., Kirshner R. P., Mandel K. S., 2011, *MNRAS*, **417**, 1280
- Bohlin R. C., Landolt A. U., 2015, *AJ*, **149**, 122
- Brown P. J., Breeveld A., Roming P. W. A., Siegel M., 2016, *AJ*, **152**, 102
- Charles P. A., Southwell K. A., O'Donoghue D., 1996, *IAU Circ.*, **6305**, 2
- Chiang E., Rappaport S., 1996, *ApJ*, **469**, 255
- Chomiuk L., et al., 2016, *ApJ*, **821**, 119
- Choudhury S., Subramaniam A., Cole A. A., Sohn Y. J., 2018, *MNRAS*, **475**, 4279
- Cowley A. P., Schmidtke P. C., Crampton D., Hutchings J. B., 1990, *ApJ*, **350**, 288
- Cowley A. P., Schmidtke P. C., Hutchings J. B., Crampton D., McGrath T. K., 1993, *ApJ*, **418**, L63
- Crampton D., Hutchings J. B., Cowley A. P., Schmidtke P. C., McGrath T. K., O'Donoghue D., Harrop-Allin M. K., 1996, *ApJ*, **456**, 320
- Di Stefano R., 2010, *ApJ*, **712**, 728
- Di Stefano R., Paerels F., Rappaport S., 1995, *ApJ*, **450**, 705
- Di Stefano R., Voss R., Claeys J. S. W., 2011, *ApJ*, **738**, L1
- Edwards Z. I., Pagnotta A., Schaefer B. E., 2012, *ApJ*, **747**, L19
- Fender R. P., Southwell K., Tzioumis A. K., 1998, *MNRAS*, **298**, 692
- Ferland G. J., et al., 2013, *Rev. Mex. Astron. Astrofis.*, **49**, 137
- Fuhrmeister B., Schmitt J. H. M. M., 2003, *A&A*, **403**, 247
- Gaia Collaboration 2018, *VizieR Online Data Catalog*, p. I/345
- Gänsicke B. T., van Teeseling A., Beuermann K., de Martino D., 1998, *A&A*, **333**, 163
- Ghavamian P., Raymond J., Hartigan P., Blair W. P., 2000, *ApJ*, **535**, 266
- Gilfanov M., Bogdán Á., 2010, *Nature*, **463**, 924
- Graczyk D., et al., 2011, *Acta Astron.*, **61**, 103
- Graur O., Woods T. E., 2019, *MNRAS*, **484**, L79
- Graur O., Maoz D., Shara M. M., 2014, *MNRAS*, **442**, L28
- Greiner J., 2000, *New Astron.*, **5**, 137
- Gruyters P., Exter K., Roberts T. P., Rappaport S., 2012, *A&A*, **544**, A86
- Hachisu I., Kato M., Nomoto K., Umeda H., 1999, *ApJ*, **519**, 314
- Hasinger G., 1994, *Reviews in Modern Astronomy*, **7**, 129
- Hoyle F., Fowler W. A., 1960, *ApJ*, **132**, 565
- Hughes J. P., et al., 1995, *ApJ*, **444**, L81
- Hutchings J. B., Cowley A. P., Mann R., Schmidtke P. C., Crampton D., 2006, in Sonneborn G., Moos H. W., Andersson B. G., eds, *Astronomical Society of the Pacific Conference Series Vol. 348, Astrophysics in the Far Ultraviolet: Five Years of Discovery with FUSE*. p. 260 ([arXiv:astro-ph/0503417](https://arxiv.org/abs/astro-ph/0503417))
- Iben I. J., Tutukov A. V., 1984, *ApJS*, **54**, 335
- Kahabka P., van den Heuvel E. P. J., 1997, *ARA&A*, **35**, 69

- Kahabka P., Pietsch W., Hasinger G., 1994, *A&A*, **288**, 538
- Kahabka P., Haberl F., Pakull M., Millar W. C., White G. L., Filipović M. D., Payne J. L., 2008, *A&A*, **482**, 237
- Kashi A., Soker N., 2011, *MNRAS*, **417**, 1466
- Kenyon S. J., Webbink R. F., 1984, *ApJ*, **279**, 252
- Kerzendorf W. E., Schmidt B. P., Asplund M., Nomoto K., Podsiadlowski P., Frebel A., Fesen R. A., Yong D., 2009, *ApJ*, **701**, 1665
- Kerzendorf W. E., Strampelli G., Shen K. J., Schwab J., Pakmor R., Do T., Buchner J., Rest A., 2018, *MNRAS*, **479**, 192
- Kosenko D., Helder E. A., Vink J., 2010, *A&A*, **519**, A11
- Kowal C. T., 1968, *AJ*, **73**, 1021
- Kuuttilla J., Gilfanov M., Seitzzahl I. R., Woods T. E., Vogt F. P. A., 2019, *MNRAS*, **484**, 1317
- Landolt A. U., 1992, *AJ*, **104**, 340
- Lang D., Hogg D. W., Mierle K., Blanton M., Roweis S., 2010, *AJ*, **139**, 1782
- Li W., et al., 2011, *Nature*, **480**, 348
- Li C.-J., et al., 2017, *ApJ*, **836**, 85
- Li C.-J., et al., 2019, arXiv e-prints, p. [arXiv:1910.01093](https://arxiv.org/abs/1910.01093)
- Livio M., Mazzali P., 2018, *Phys. Rep.*, **736**, 1
- Long K. S., Helfand D. J., Grabelsky D. A., 1981, *ApJ*, **248**, 925
- Lundqvist P., et al., 2020, arXiv e-prints, p. [arXiv:2001.06070](https://arxiv.org/abs/2001.06070)
- Moll R., Raskin C., Kasen D., Woosley S. E., 2014, *ApJ*, **785**, 105
- Nielsen M. T. B., Gilfanov M., 2015, *MNRAS*, **453**, 2927
- Nielsen M. T. B., Dominik C., Nelemans G., Voss R., 2013, *A&A*, **549**, A32
- Nomoto K., 1982, *ApJ*, **253**, 798
- Nomoto K., Sugimoto D., Neo S., 1976, *Ap&SS*, **39**, L37
- Nomoto K., Saio H., Kato M., Hachisu I., 2007, *ApJ*, **663**, 1269
- Nugent P. E., et al., 2011, *Nature*, **480**, 344
- Orio M., Zezas A., Munari U., Siviero A., Tepedelenioglu E., 2007, *ApJ*, **661**, 1105
- Osterbrock D. E., Ferland G. J., 2006, *Astrophysics of gaseous nebulae and active galactic nuclei*. "United Science Books"
- Patat F., et al., 2007, *Science*, **317**, 924
- Pellegrini E. W., Oey M. S., Winkler P. F., Points S. D., Smith R. C., Jaskot A. E., Zastrow J., 2012, *ApJ*, **755**, 40
- Perlmutter S., et al., 1999, *ApJ*, **517**, 565
- Polin A., Nugent P., Kasen D., 2019, *ApJ*, **873**, 84
- Rajoelimanana A. F., Charles P. A., Meintjes P. J., Odendaal A., Udalski A., 2013, *MNRAS*, **432**, 2886
- Rappaport S., Chiang E., Kallman T., Malina R., 1994, *ApJ*, **431**, 237
- Raskin C., Kasen D., Moll R., Schwab J., Woosley S., 2014, *ApJ*, **788**, 75
- Reinsch K., van Teeseling A., Beuermann K., Thomas H. C., 1996, in Zimmermann H. U., Trümper J., Yorke H., eds, *Roentgenstrahlung from the Universe*. pp 183–184
- Remillard R. A., Rappaport S., Macri L. M., 1995, *ApJ*, **439**, 646
- Rest A., et al., 2005, *Nature*, **438**, 1132
- Rest A., et al., 2008, *ApJ*, **681**, L81
- Rest A., et al., 2014, *ApJ*, **795**, 44
- Riess A. G., et al., 1998, *AJ*, **116**, 1009
- Rosswog S., Kasen D., Guillochon J., Ramirez-Ruiz E., 2009, *ApJ*, **705**, L128
- Ruiter A. J., 2020, arXiv e-prints, p. [arXiv:2001.02947](https://arxiv.org/abs/2001.02947)
- Ruiz-Lapuente P., 2018, arXiv e-prints, p. [arXiv:1812.04977](https://arxiv.org/abs/1812.04977)
- Ruiz-Lapuente P., et al., 2004, *Nature*, **431**, 1069
- Schaefer B. E., Pagnotta A., 2012, *Nature*, **481**, 164
- Schaeidt S., Hasinger G., Truemper J., 1993, *A&A*, **270**, L9
- Schmidtke P. C., Cowley A. P., 1995, *IAU Circ.*, **6278**, 2
- Schmidtke P. C., Cowley A. P., Crane J. D., Taylor V. A., McGrath T. K., Hutchings J. B., Crampton D., 1999, *AJ*, **117**, 927
- Sienkiewicz R., 1980, *A&A*, **85**, 295
- Someya K., Bamba A., Ishida M., 2014, *PASJ*, **66**, 26
- Spector O., Finkelman I., Brosch N., 2012, *MNRAS*, **419**, 2156
- Starrfield S., Timmes F. X., Hix W. R., Sion E. M., Sparks W. M., Dwyer S. J., 2004, *ApJ*, **612**, L53
- Walker A. R., 2012, *Ap&SS*, **341**, 43
- Waller W. H., 1990, *PASP*, **102**, 1217
- Wang L., Wheeler J. C., 2008, *ARA&A*, **46**, 433
- Webbink R. F., 1984, *ApJ*, **277**, 355
- Wheeler J. C., Hansen C. J., 1971, *Ap&SS*, **11**, 373
- Williams B. J., et al., 2014, *ApJ*, **790**, 139
- Wolf W. M., Bildsten L., Brooks J., Paxton B., 2013, *ApJ*, **777**, 136
- Woods T. E., Gilfanov M., 2016, *MNRAS*, **455**, 1770
- Woods T. E., Ghavamian P., Badenes C., Gilfanov M., 2017, *Nature*, **1**, 800
- Woods T. E., Ghavamian P., Badenes C., Gilfanov M., 2018, *ApJ*, **863**, 120
- Zaritsky D., Harris J., Thompson I. B., Grebel E. K., 2004, *AJ*, **128**, 1606
- van den Heuvel E. P. J., Bhattacharya D., Nomoto K., Rappaport S. A., 1992, *A&A*, **262**, 97
- van der Heyden K. J., Behar E., Vink J., Rasmussen A. P., Kaas-stra J. S., Bleeker J. A. M., Kahn S. M., Mewe R., 2002, *A&A*, **392**, 955

This paper has been typeset from a $\text{\TeX}/\text{\LaTeX}$ file prepared by the author.